Microstructure and corrosion behavior of differently heat-treated Ti-6Al-4V alloy processed by laser powder bed fusion of hydride-dehydride powder

Melody H. Delpazir ^a, Mohammadreza Asherloo ^a, Sajjad Nasiri Khalil Abad ^b, Alaina Thompson ^C, Victor Guma ^a, Sourabh D. Bagi ^a, Keerthi Kumar Sreenivas ^a, Muktesh Paliwal ^d, Jeff Terry ^C, Anthony D. Rollett ^e, Amir Mostafaei ^{a, *}

- ^a Department of Mechanical, Materials and Aerospace Engineering, Illinois Institute of Technology, 10 W 32nd Street, Chicago, IL 60616, USA
- ^b Cummins Inc., Nijverheidsstraat 48c, 2260, Oevel, Belgium
- ^c Department of Physics, Illinois Institute of Technology, 3101 S. Dearborn St., Chicago, Illinois 60616
- ^d Kymera International Reading Alloys, Robesonia, PA 19551, USA
- ^e Department of Materials Science and Engineering, Carnegie Mellon University, Pittsburgh, PA 15213, United States
- * Corresponding authors: A. Mostafaei (mostafaei@iit.edu)

Abstract

This study investigates the use of hydride-dehydride non-spherical Ti-6Al-4V powders in laser powder bed fusion process and the effects of post-heat-treatments on additively manufactured parts. As-built parts show anisotropic microstructure with α' martensite and some β phases. Post heat-treated parts exhibit $\alpha+\beta$ phases, with characteristics dependent on the heat treatment. Heat treatment below β -transus leads to homogenized grain structures with improved corrosion resistance. Electrochemical analysis reveals a very stable corrosion rate due to faster formation of a protective passive layer aided by the fine-structured β phase. X-ray photoelectron spectroscopy examines corrosion behavior and film growth mechanism in saline water.

Keywords: Additive manufacturing; Titanium; Heat treatment; Passive film; XPS.

1. Introduction

Powder bed fusion (PBF) processes have garnered substantial attention across various industries due to the multitude of advantages they offer over traditional manufacturing techniques. These benefits encompass exceptional design flexibility, diminished post-processing requirements, and minimized material wastage [1]. The Ti-6Al-4V alloy stands out as a particularly well-suited material for PBF methods such as laser or electron beam techniques, primarily due to its outstanding weldability [2]. This alloy is in high demand owing to its highly favorable attributes, including remarkable strength, biocompatibility, and corrosion resistance [1,2].

Traditionally, conventional feedstock for the Ti-6Al-4V alloy was prepared using melting methods like plasma rotating electrode processes and atomization [3], resulting in the formation of spherical powder morphology. The use of spherical particles in powder bed additive manufacturing (AM) is deemed crucial owing to their capacity to enhance powder flow, spreadability, packing density, and reproducibility. These advantages ultimately contribute to the improvement of final part density and overall performance [1,4–7]. Fusion-based AM methods, including laser or electron beam powder bed fusion (L-PBF or EB-PBF), predominantly rely on spherical atomized powders, despite concerns related to entrapped gas within particles and the costs associated with powder production.

In recent times, a misconception has arisen that non-spherical particles are unsuitable for achieving fully dense parts through L-PBF. Nevertheless, technological advancements have led to

the commercialization of several cost-effective powder production methods [8,9]. These techniques involve refining recycled metal scrap, machine turnings, or milled sponge in conjunction with blended elements. Non-spherical powders offer notably greater cost efficiency, with costs reduced by approximately 40-50% compared to pre-alloyed powders possessing spherical morphologies produced by atomization [9–13].

The hydride-dehydride (HDH) process represents an economical production method that employs hydrogen as a temporary alloying element, presenting more environmentally friendly alternatives. Some studies have explored the application of non-spherical HDH Ti-6Al-4V powder in powder bed fusion (PBF) processes. For instance, Varela et al. [14] achieved a relative density exceeding 98.9% using HDH Ti-6Al-4V powder with particle sizes ranging from 50-120 μ m in the L-PBF process. Narra et al. [15] utilized HDH Ti-6Al-4V powder with particle sizes of 75-175 μ m in the EB-PBF process, resulting in a final relative density surpassing 99%. Wu et al. [16] and Asherloo et al. [17] optimized the L-PBF process for HDH Ti-6Al-4V powder, attaining a relative density of 99.9%. These studies demonstrated the capacity to manipulate the grain structure, influencing the size of the α' martensite phase and the morphology of the prior β grains. Moreover, the utilization of coarser HDH powder in L-PBF can increase the build rate by 1.5-2 times compared to commercially available machines employing spherical powder (15-45 μ m).

The investigation into the electrochemical behavior and corrosion resistance of Ti-6Al-4V samples processed through fusion-based additive manufacturing (AM) seeks to unravel the influence of the manufacturing process on microstructure and corrosion tendencies. Factors such as cooling rate, melt pool size, and solidification rate, all affected by the fusion-based AM process, play a pivotal role in shaping the final microstructure of Ti-6Al-4V alloys. Laser-based techniques, such as laser beam direct energy deposition (LB-DED) and L-PBF, yield prior β grains and an acicular α' martensite phase due to rapid cooling rates. The high cooling rate limits the time available for diffusional transformation, resulting in the formation of non-equilibrium fine acicular martensite (α' phase) and large-size columnar grain (prior β grains) due to successive layer-by-layer fabrication [18]. Additionally, non-uniform thermal stress, known as residual stress, arises from temperature fluctuations. This combination of α' phase, columnar grain, and residual stress renders LB-PBF Ti-6Al-4V brittle, less ductile, and anisotropic. Hence, optimizing microstructures and properties is imperative for different applications [19]. In contrast, the EB-PBF process results in a fine $\alpha+\beta$ dual-phase microstructure due to a slower cooling rate when compared to L-PBF [20].

Post-thermal treatment effectively adjusts microstructures, properties, and residual stress in titanium alloys [21]. Residual stress relaxation occurs at relatively low temperatures, with phase transformations observed at higher temperatures [22]. In the range of 750–900 °C, the acicular α' phase transforms into a mixed α and β phase microstructure. Beyond the β transition temperature (about 995 °C), the β phase entirely replaces α' phase and prior columnar β grain. However, the full extent of micro/nano-structural evolution, including element diffusion and quantitative phase analysis, demands further exploration. Researchers have evaluated the electrochemical behavior of fusion-based AM processed Ti-6Al-4V powder in various manufacturing states, encompassing as-built and post-heat-treated conditions. Contradictory electrochemical responses have been documented, attributed to variances in thermal cycles, microstructure, and phase fractions within the tested materials [21–36]. Hence, it is imperative to methodically characterize both microstructure and corrosion behavior when devising a new powder specification alongside optimal L-PBF process parameters.

In a prior study by Asherloo et al. [17], a process window for the L-PBF technique utilizing HDH Ti-6Al-4V powder was identified, enabling the fabrication of near fully dense parts. This study delved into a comprehensive analysis of the microstructure and electrochemical behavior of these high-density components, comparing their attributes against specimens subjected to distinct heat treatments. The results were meticulously elucidated and compared to existing literature, effectively considering the intricate interplay between powder characteristics, manufacturing process parameters, resulting structures, defects, and material properties.

2. Experimental procedures

2.1 Materials and manufacturing process

In this research, hydride-dehydride non-spherical Ti-6Al-4V powder from Reading Alloys (Kymera International) was used. The particle had a size in the range 50-120 µm as shown in Figure 1A. Blocks with dimensions of 20 mm × 20 mm × 60 mm (see Figure 1B) were fabricated using an L-PBF machine (model EOS M290) with an optimized process parameters given in our earlier study [17]. The as-built parts were subjected to stress relief at 650 °C for 2 h. Subsequently, the parts were removed from the baseplate using a wire electrical discharge machining tool.

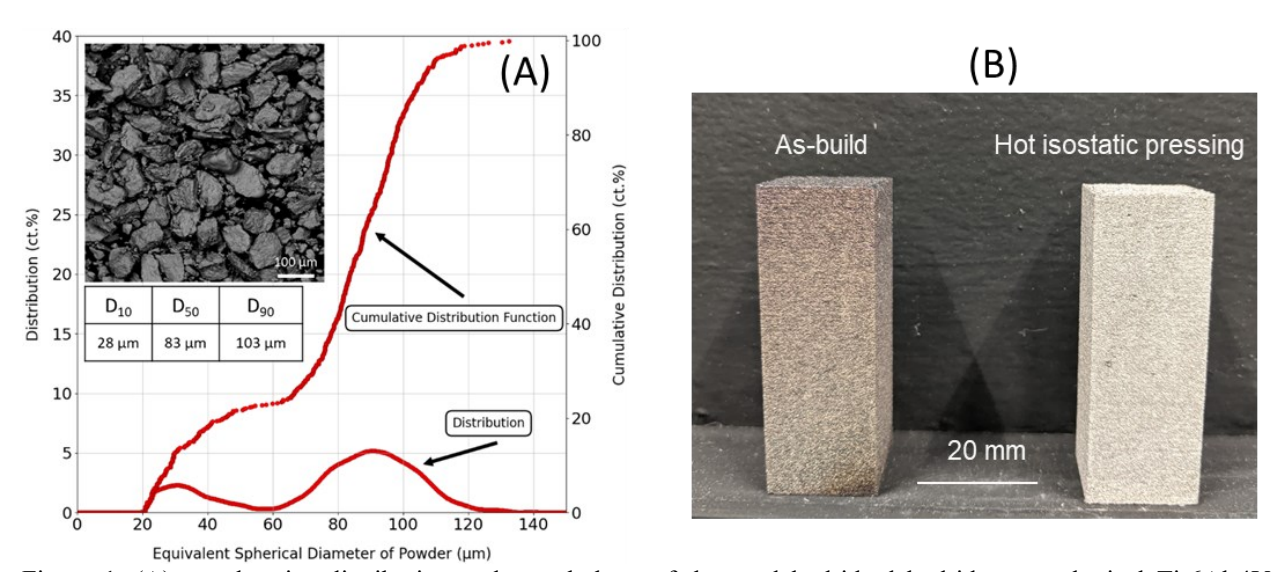


Figure 1. (A) powder size distribution and morphology of the used hydride-dehydride non-spherical Ti-6Al-4V powder [37], and (B) examples of L-PBF processed blocks for this study.

2.2 Post processing and sample preparations

Three distinct heat-treatment procedures were employed on the fabricated as-built (AB) samples. Two of the samples underwent heat treatment at temperatures of 850 ± 2 °C (HT1) and 1045 ± 2 °C (HT2) for 2 h, followed by furnace cooling with a rate of 1.7 °C/min. These temperature levels represent different ranges above and below the $\beta_{transus}$ temperature (995 °C) [38]. The third condition involved subjecting the samples to hot isostatic pressing (HIP) at 899 °C \pm 14 °C and a pressure of 1034 ± 34 bar for 2 h, followed by water quenching. To examine the microstructure and texture, samples were prepared from the vertical (xz) and horizontal (xy) directions. For optical microscopy observations, the samples were hot mounted then ground up to 2400 grit SiC paper, polished with a 1 μ m Alumina solution, and etched with Kroll's reagent. For texture analysis, samples were ground to using a 800-grit SiC paper, then polished with 1 μ m and

 $0.05~\mu m$ alumina solutions, and finally polished with $0.04~\mu m$ colloidal silica. For electrochemical testing, samples with surface area of 20 mm \times 20 mm were connected to wire and cold mounted, then ground up to 1200-grit SiC paper prior to the electrochemical tests.

2.3 Material Characterization

For optical microscopy observations, a VHX 7100 Keyence microscope was used. A JEOL 5900LV scanning electron microscope (SEM) equipped with an electron backscattered diffraction (EBSD, Oxford Instruments) was employed. AzTec software was used for data collection at the operational accelerating voltage and step size were 20 keV and 0.5 μm, respectively. Post-processing was performed on the raw EBSD data using HKL Channel 5 software package. MTEX, a MATLAB-based toolbox [39], was used to reconstruct grains and do grain/texture analysis. An X-ray diffraction machine (model ARL XTRA X-ray diffractometer) was used for phase analysis equipped with Cu-Kα radiation at an accelerative voltage and current of 35 kV and 30 mA, respectively. The 2θ range was 20-100° with a scan rate of 1 s/step and scan step size of 0.02°. To extract crystallography parameters, the collected XRD data was analyzed using MAUD software.

2.4 Electrochemical Measurement

Electrochemical studies such as (i) open circuit potential (OCP), (ii) potentiodynamic polarization (PD), and (iii) electrochemical impedance spectroscopy (EIS) were carried out on samples using a conventional three-electrode cell connected to a computer-controlled impedance instrument (Gamry Instruments, Interface 1010E potentiostat). The working electrodes were mounted samples with an effective surface area of 1 cm². The counter electrode was a graphite rod and the reference electrode was an Ag/AgCl electrode saturated with 3M KCl. Experiments were conducted in a 3.5 wt.% NaCl solution at ambient temperature. The specimens were placed in saline water for 3600 s to stabilize the surface chemistry. EIS measurements were performed with an AC amplitude of 10 mV and frequencies ranging from 10⁵ to 10⁻² Hz and the Gamry Echem Analyst software was used to analyze data. Potentiodynamic polarization measurements were conducted within the potential range of -0.5-2.5 V at a scan rate of 1 mV/s. All the electrochemical tests were repeated more than three times.

2.5 XPS analysis after electrochemical test

The Ti thin film was studied using a Phi 5600 XPS system. Monochromated Al-K α = 1486.6 eV x-rays were used to study the sample. The spectra were referenced to the C 1s spectra of adventitious carbon present in the sample at a binding energy (BE) of 285.02 eV. A depth profile was done using Ar ion sputtering, at a beam voltage of 1 kV over various intervals until 300 s of total sputtering was done, which is when the electrochemical corrosion film appeared to be gone. The core level BE scans were taken with E_{pass} of 23.5 eV, step size of 0.05 eV, and dwell time of 0.1 s. The data was fitted using Gaussian-Lorentzian peaks with ratio of 70:30, and Gaussian-Lorentzian asymmetric lineshapes for Ti⁰ with $\alpha = 1.1$, $\beta = 5$, and a Gaussian of width characteristic of m = 7 [40]. The spin-orbit splitting for Ti²⁺, Ti³⁺, Ti⁴⁺, and Ti⁰ were approximately 5.73, 5.60, 5.66, and 6.13 eV, respectively [41]. The spin orbit area ratio was held at 2:1. An iterative Shirley background was used to fit all the photopeaks.

3. Results and Discussion

- 3.1 Microstructural observations
- 3.1.1 Optical microscopy

Figure 2 shows the microstructure of the as-built (with a relative density of 99.94 % measured using 2D image analysis and Archimedes principle [17]) and post heat-treated L-PBF processed HDH Ti-6Al-4V samples obtained by optical microscopy. The optical micrographs of the AB samples demonstrated columnar prior β grain in the xz plane associated with the preferential solidification in L-PBF process due to heat transfer orientations in the melt pool, and grain growth toward the build direction (e.g., of <001> direction). On the xz plane, prior β grains with a width of 85 ± 35 µm grew over multiple deposited layers with several millimeters in length. However, cross-sections in the xy plane showed equiaxed prior β grains associated with the scan strategy. High magnification optical micrographs of the AB specimens revealed a large fraction of acicular a' martensite with the length of several tens to hundreds of micrometers in the microstructure of the L-PBF processed Ti-6Al-4V alloy. It is known that the high cooling rate associated with the laser melting processes (~5600-6500 °C/s [42]) results in non-equilibrium transformation of β to α' . Also, small scale melt pool size (e.g., 70-300 µm) leads to a high thermal gradient of ~10⁵ °C/s along the build direction, results in a non-equilibrium cooling condition. These are two main reasons of acicular α' martensite formation rather than the equilibrium α phase in Ti-6Al-4V alloy [26,32,43]. Presence of nano scale β phase up to \sim 2 % is possible in the AB specimens due to the cyclic thermal history [42,44].

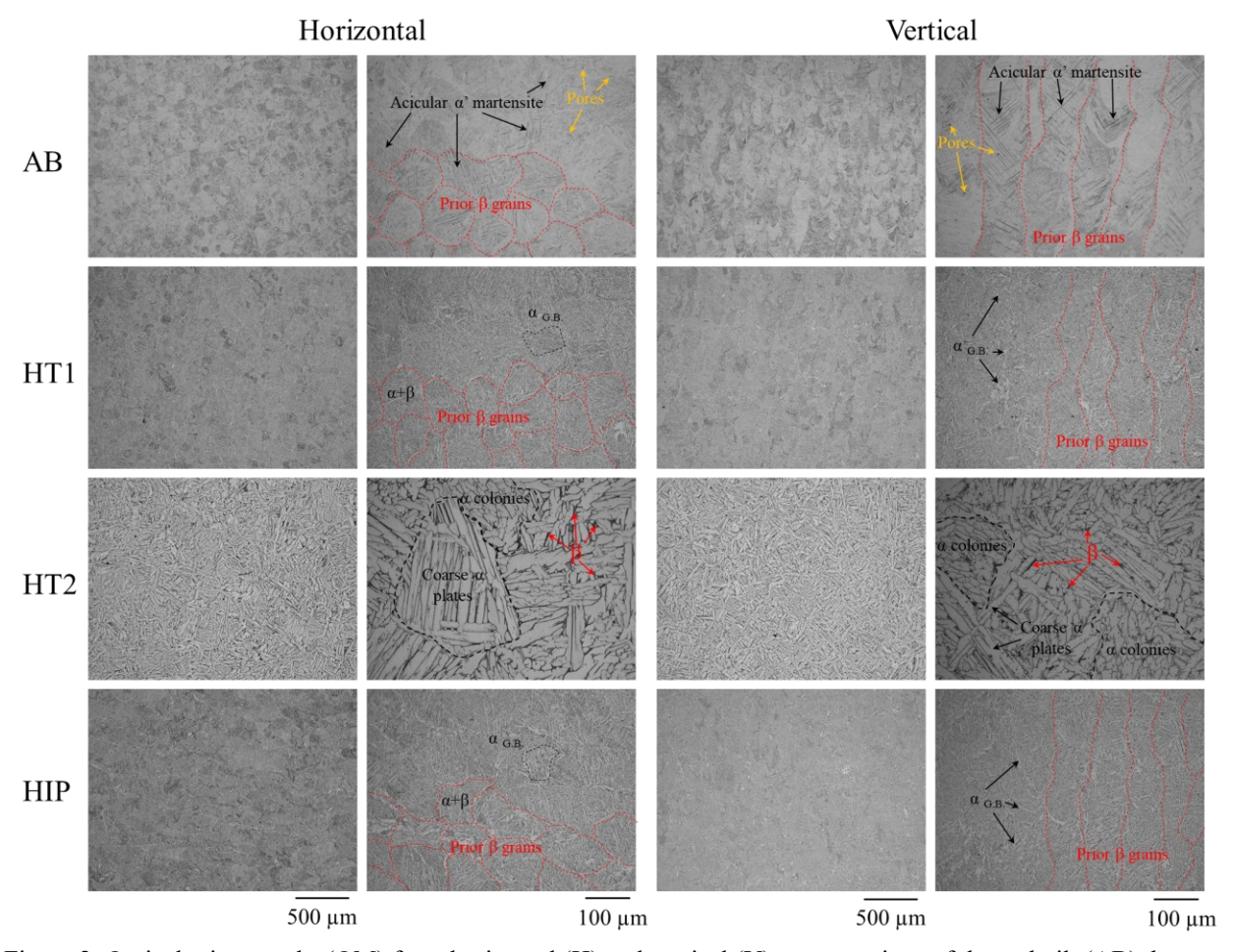


Figure 2. Optical micrographs (OM) from horizontal (H) and vertical (V) cross-sections of the as-built (AB), heat-treated at 850 °C (HT1), and heat-treated at 1045 °C (HT2), and hot isostatically pressed at 900 °C (HIP) L-PBF processed HDH Ti-6Al-4V parts.

The post heat-treatments of hot isostatically pressing (899 °C - HIP), sub- (850 °C - HT1) and above (1045 °C - HT2) $\beta_{transus}$ temperature evolved microstructure of the as-deposited L-PBF processed Ti-6Al-4V samples. As indicated in Figure 2, the grain structure was unchanged after HIP and HT1 treatments in which the prior β grains with columnar and equiaxed structure were seen in the xz and xy sections, respectively. At higher magnifications on the optical micrographs of the HIP and HT1 cross-sections, the acicular α' martensite structure was transformed into the α phase surrounded by β crystal precipitates due to segregation of V element. When lamellar $\alpha + \beta$ phases formed in the prior β grains, the resultant microstructure was a fine basket-weave microstructure. Moreover, continuous columnar (on xz plane) or equiaxed (on xy plane) grain boundary α phase ($\alpha_{G.B.}$) was evident in both HIP and HT1 conditions, indicating that the intrinsic morphologies of the prior β grains did not evolve by the sub $\beta_{transus}$ heat-treatments [25,31,45,46]. α grains within the prior β grains were in the range 2-125 μ m.

For heat-treatment above the β_{transus} temperature (1045 °C – HT2), microstructure evolution was significant such that a typical lamellar $\alpha + \beta$ microstructure was observed in prior β gains with a diameter ranging ~300-700 µm and α plate colonies with lath lengths up to several hundred micrometers and width of ~ 20 µm. Heat-treatment at 1045 °C caused the acicular α' martensite to transform to β phase. For a slow furnace cooling rate of 1.7 °C/min, transformation of $\beta \rightarrow \alpha$ occurred, thus lamellar $\alpha + \beta$ phases formed in the equiaxed prior β grains. Although all the post heat-treatments (HIP, HT1, HT2) resulted in formation of a lamellar microstructure, the α lath width was significantly finer for the lower temperature HIP and HT1 heat treatments.

3.1.2. Scanning electron microscopy

Figure 3 showed SEM micrographs of the as-built and post-heat treated samples. As mentioned before, α' martensite dominates in the as-built sample (see Figure 3) with a small fraction of β nano particles. As reported by Yu et al. [47], the $\alpha' \to \alpha + \beta$ process requires diffusion, thus the position and shape of the precipitations can be controlled with dwell time and peak temperature. The martensitic decomposition starts above 400 °C and by increasing the temperature, the fraction of decomposed α' martensite increases [48]. Moreover, the β phase forms initially as nano-scale particles which then evolves to short needle morphology with increasing temperature; the present study confirmed this phenomenon. High magnification micrographs of the as-built condition (i.e., stress relieved at 650 °C for 2h) showed randomly dispersed nano-scale granular β phase. Additional post-process heat-treatment at 850 °C for 2h (HT1) converted some of the particles into small needles. Heat treatment above the β_{transus} temperature (HT2) converted all α' to β phase and, on slowly cooling, a large fraction of the β transformed to α phase; the remaining β was stabilized via enrichment in V. Because of the complete transformation to β phase during the heating cycle above the β_{transus} , equiaxed prior β grains formed, followed by $\beta \rightarrow \alpha$ transformation on cooling below the β_{transus} . Also, α formed both within grains and at prior β grain boundaries. Hot isostatic pressing (HIP, ~900 °C for 2h under 100 MPa) led to complete aggregation of granular β to form longer needle shaped β at the grain boundaries. The decomposition of α' martensite resulted in formation of lamellar $\alpha + \beta$ phase within the prior β grain, however, the columnar prior β grains remained unchanged (see Figure 2). The brighter needle-shaped features in SEM micrographs of as-built condition were labeled as α' martensite because these are V-enriched [49], i.e., higher (average) atomic number than the matrix. The same argument was made for the heat-treated samples. Brighter regions in the SEM micrographs denote V-enriched regions, assumed to be β .

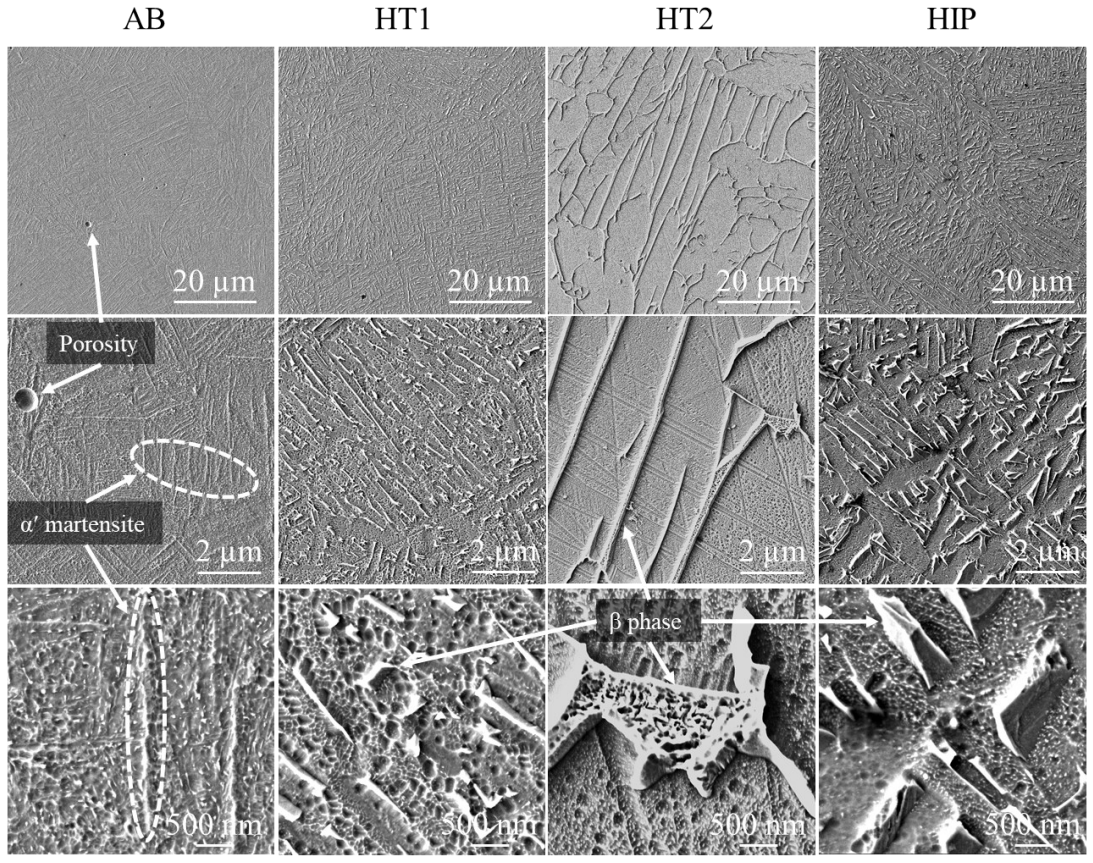


Figure 3. Scanning electron micrographs from the cross-sections of samples in as-built + stress relieved at 650 °C for 2h (AB), heat-treated at 850 °C for 2h (HT1), heat-treated at 1045 °C for 2h (HT2), and hot isostatically pressed (HIP, ~900 °C for 2h under 100 MPa) conditions. The first, second, and third rows showed micrographs at 500X, 2,000X, and 10,000X magnifications, respectively.

To study the microstructure and texture evolution in manufactured parts, EBSD analysis was conducted. Figure 4 shows inverse pole figure maps (IPF-Z) and reconstructed prior β grains on both xz and xy sections. Reconstruction of β grains used the established Burgers orientation relationship between the α' and (parent) β , i.e., $[0001]_{\alpha} \parallel [110]_{\beta}$ and $[2\ \bar{1}\ \bar{1}\ 0]_{\alpha} \parallel [\bar{1}\ 1\ \bar{1}]_{\beta}$. In the xz section, the presence of columnar grains was obvious, reflecting the layer wise deposition process of L-PBF and the regrowth of grains from previously deposited layers into the new ones. However, interruptions in grain regrowth were observed in the vertical cross-section, which can be attributed to two factors: (1) the scan rotation of 67° and (2) instability and non-uniform thermal gradient within the melt pool [50]. These factors account for the variation in orientation of the prior β grains after the deposition of new layers, resulting in what is commonly known as stray grains [51]. On the xy section, the EBSD pole figure (see Figure 4) indicates a random texture. Columnar grain growth is expected in L-PBF processed alloys using a laser scan rotation of 0° or 0° [52]. However, applying a laser scan rotation of 0° produced a more random distribution, thereby reducing the texture in the L-PBF processed parts. This directly impacts the corrosion behavior of L-PBF processed materials as we will describe.

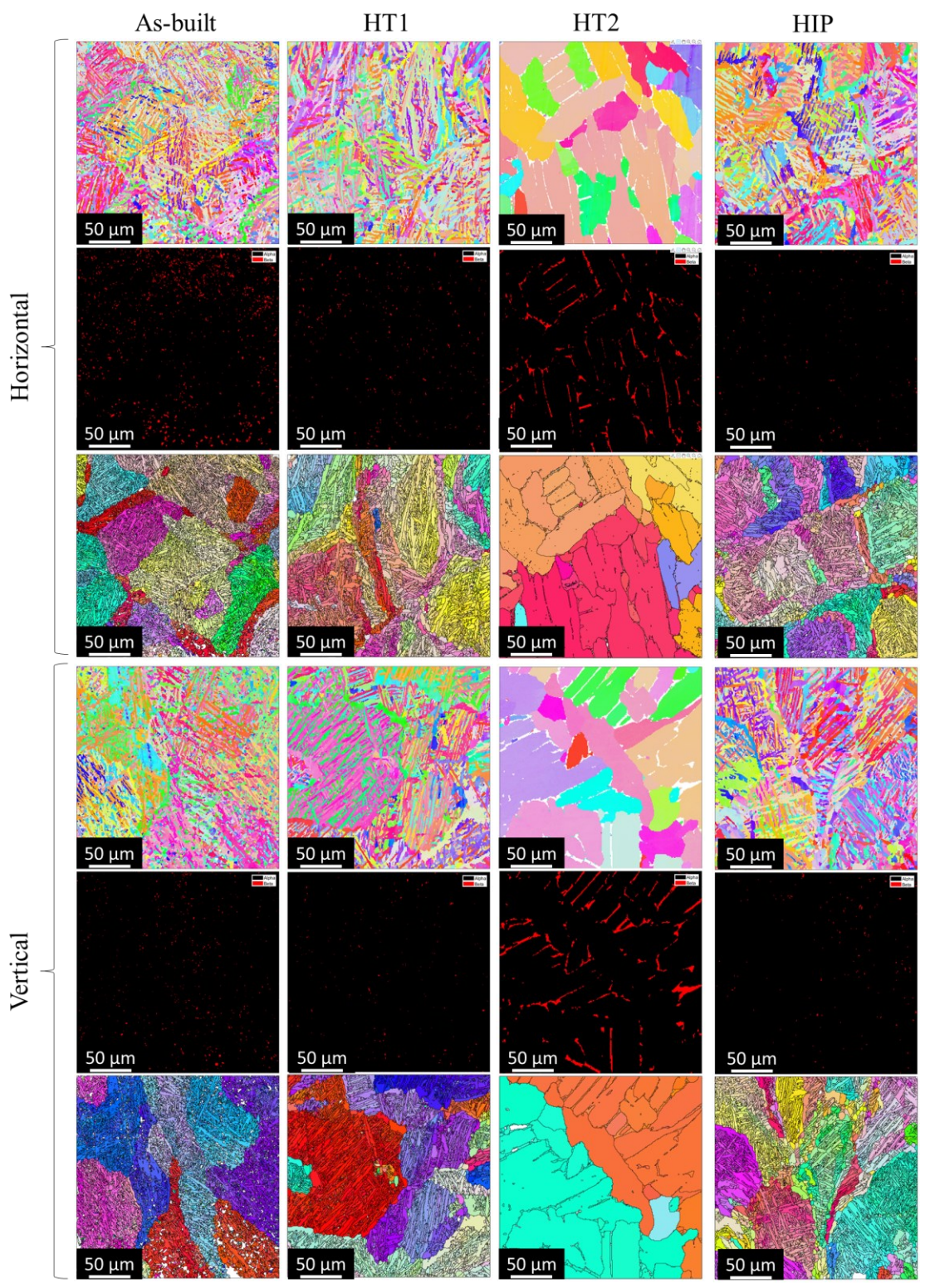


Figure 4. (First row) IPF maps, (second row) phase maps, and (third row) reconstructed prior β grains extracted from the EBSD data of vertical and horizontal cross-sections of each heat-treatment condition. In HT2 samples, a higher fraction of β phase and grain coarsening are seen in phase maps and reconstructed prior β grains, respectively.

EBSD data was acquired for the different heat-treated conditions was carried out to quantify the microstructural evolution of the parts, Figure 4. The IPF maps show minor change in α/α' lath spacings (see below) after HT1 (850 °C for 2h) and HIP (900 °C for 2h under 100 MPa) processes. On the other hand, HT2 (1045 °C for 2h) resulted in significant coarsening of the lamellar $\alpha+\beta$. As mentioned before, cooling slowly below the β_{transus} temperature results in large α laths along with large lath shaped β phase (see Figure 3). Measurement of α/α' lath width using EBSD data revealed slightly wider α/α' laths after HT1 (averaged 1.83 μ m) and HIP (averaged 2.25 μ m) processes compared to as-built (averaged 1.45 μ m) condition. Also, no significant difference was observed between the α/α' lath width in xz and xy sections. Once more, the completely different α lath formation after HT2 heat-treatment was confirmed by the significantly higher average α lath size of 28.19 μ m (see Figure 5).

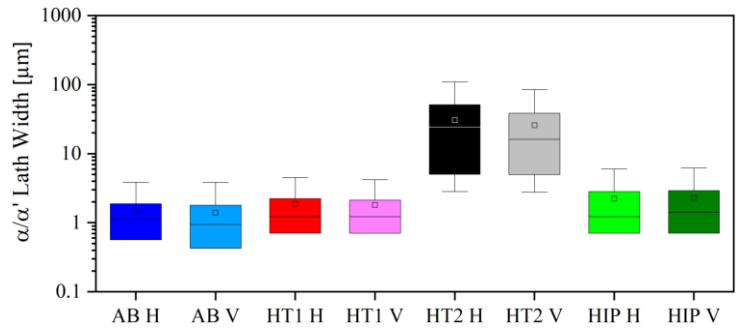


Figure 5. α/α' lath width measured using the EBSD data for vertical and horizontal cross-sections of each heat-treatment condition. Numbers on top of each box plot show the average lath width in each condition.

Further microstructural investigations were carried out to understand the influence of heat-treatment on the microstructure of the L-PBF processed Ti-6Al-4V parts. The Burgers relationship governing the hexagonal closed packed (HCP) to body centered cubic (BCC) transformation [53], causes α/α grain boundaries in titanium alloys to be one of the types summarized in Table 1 based on the calculations by Wang *et al.* [54] and Gey *et al.* [55] that are considered high angle grain boundaries (HAGB).

Table 1. List of α/α boundary types expected from the Burgers orientation relationship between BCC and HCP crystal structures in titanium. Type 1 corresponds to two identical or similar α lath orientations resulting in a low angle grain boundary; these were not analyzed quantitatively in this study.

α/α boundary type	Misorientation angle (°)	Misorientation axis
2	60	$[1 \ 1 \ \overline{2} \ 0]$
3	60.83	$[\overline{1.377}\ \overline{1}\ 2.377\ 0.359]$
4	63.26	$[\overline{10}\ 5\ 5\ \overline{3}]$
5	90	$[1\ \overline{2.38}\ 1.38\ 0]$
6	10.53	[0 0 0 1]

The Type 1 α/α boundary is a low angle grain boundary (LAGB) between two closely oriented α grains. The relative frequency of misorientations (reduced to angle) between α grains reveals the distribution of these types, see Figure 6a,b. Heat-treating samples below the $\beta_{transus}$ temperature (i.e., HT1 and HIP) does not affect the misorientation distribution between the α grains; however, when the samples are heat-treated above the $\beta_{transus}$, the main peak shifts from ~65° to ~60° which

is an obvious change of α/α boundary type, i.e., HT2 is the only heat treatment that changes the distribution.

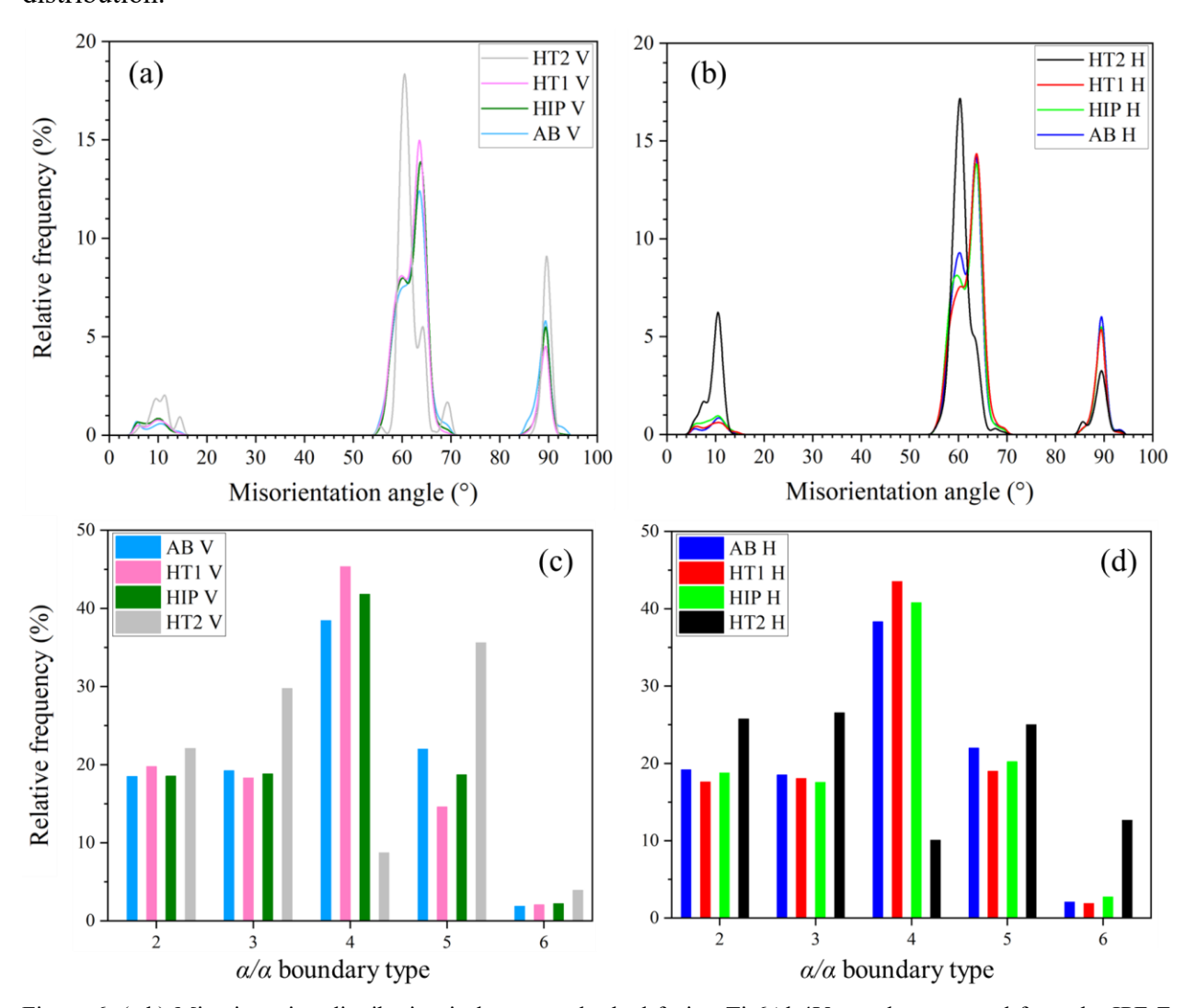


Figure 6. (a,b) Misorientation distribution in laser powder bed fusion Ti-6Al-4V powder extracted from the IPF-Z maps of EBSD micrographs after various heat-treatments. (c,d) α/α boundary type distribution calculated based on the misorientation distribution extracted from the EBSD data.

Figure 6c,d shows the distribution of each α/α boundary type by sample. The dominance of type 4 in the as-built specimen is due to the high cooling rates associated with the L-PBF process as reported in Refs. [56,57]. The same dominance of type 4 persists in HT1 and HIP. This is because the orientation of α grains does not change at temperatures below β_{transus} (see Figure 7a), instead, only the V atoms diffuse out of the α' laths to form β phase and the Al atoms diffuse in, thus thickening the α laths. However, for heat-treatment above the β_{transus} , all of the α' laths transform to β phase. While cooling down through the β_{transus} , new and larger α grains nucleate and grow during the $\beta \rightarrow \alpha$ solid state transformation. This fresh nucleation of α grains will force the material to go through a new variant selection process and have completely different distribution of α/α boundary types [58,59].

The effect of post heat-treatment on the anisotropy of the parts was examined, see Figure 7, and the maximum pole density was extracted from each pole figure and plotted against the heat-

treatment temperature. As expected, there is negligible difference between the pole densities of α grains in the xy and xz sections, regardless of the heat-treatment temperature. As stated before, the heat-treatment below β_{transus} does not change the α grain orientations, however, heat-treatment above the β_{transus} changes the α grain orientations drastically which is attributed to the fact that above β_{transus} , all the α grains transform to beta and new α grains nucleate during the $\beta \rightarrow \alpha$ transformation. Orientation of prior β grains, however, demonstrated different behavior compared to the α grains. Vertical cross-sections had higher anisotropy compared to the horizontal cross-sections when the samples were heat-treated below the β_{transus} temperature because this does not change the columnar growth of the beta from printing. By heat-treating the samples above the β_{transus} temperature, however, the change in prior β grains texture is significant.

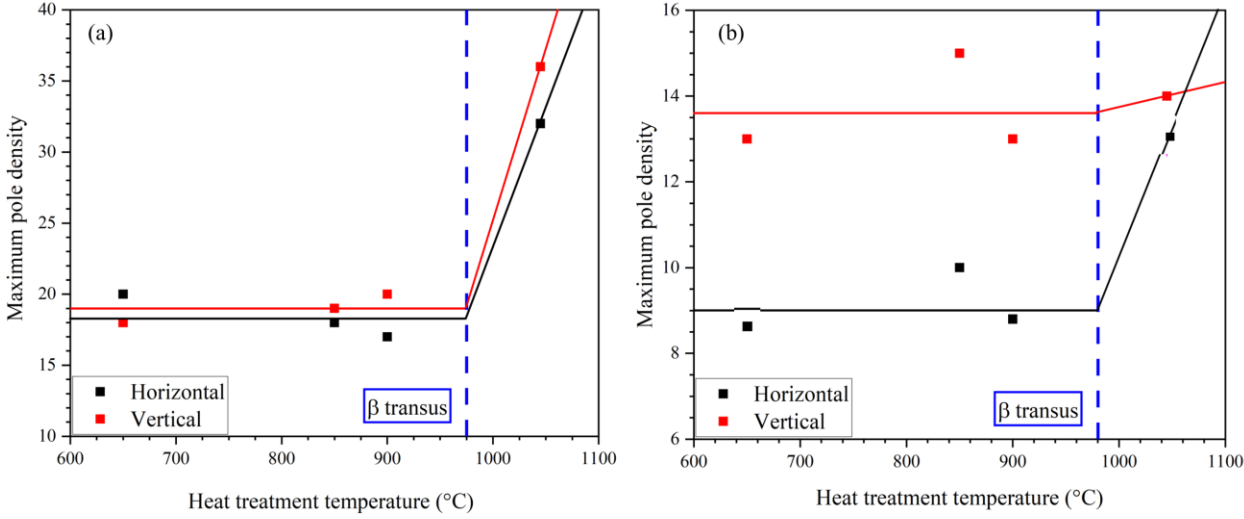


Figure 7. The extracted maximum pole density from the (a) HCP $\{0001\}$ pole figure, and (b) BCC $\{001\}$ pole figure. The blue dashed line in both plots denotes the β_{transus} temperature based on Ref. [60].

3.2 Phase analysis using X-ray diffraction

Figure 8a displays the XRD patterns and corresponding index peaks obtained from the asbuilt and differently post heat-treated samples. The peak positions in the post heat-treated specimens shifted slightly towards lower 2θ values, suggesting an increase in lattice parameter. Both α and α' phases have an HCP crystal structure, hence the collected XRD patterns remain the same with slight variations in the lattice parameters and their ratio. Thus, the α phase becomes more dominant due to α' decomposition into $\alpha+\beta$. During the high cooling rate of the L-PBF process, the diffusion of V in the solid solution is suppressed, albeit not entirely. This diffusionless transformation results in a V-rich supersaturated martensite phase. Consequently, the post heat-treatment process facilitates the diffusion of V to the β phase, which has a higher capacity for V dissolution compared to the α and α' phases. As a result, a gradual convergence from α' to α phase occurs, accompanied by an increase in the proportion of the β phase [25,26,29,30,61]. More detailed analysis of the XRD results will be available in a forthcoming paper.

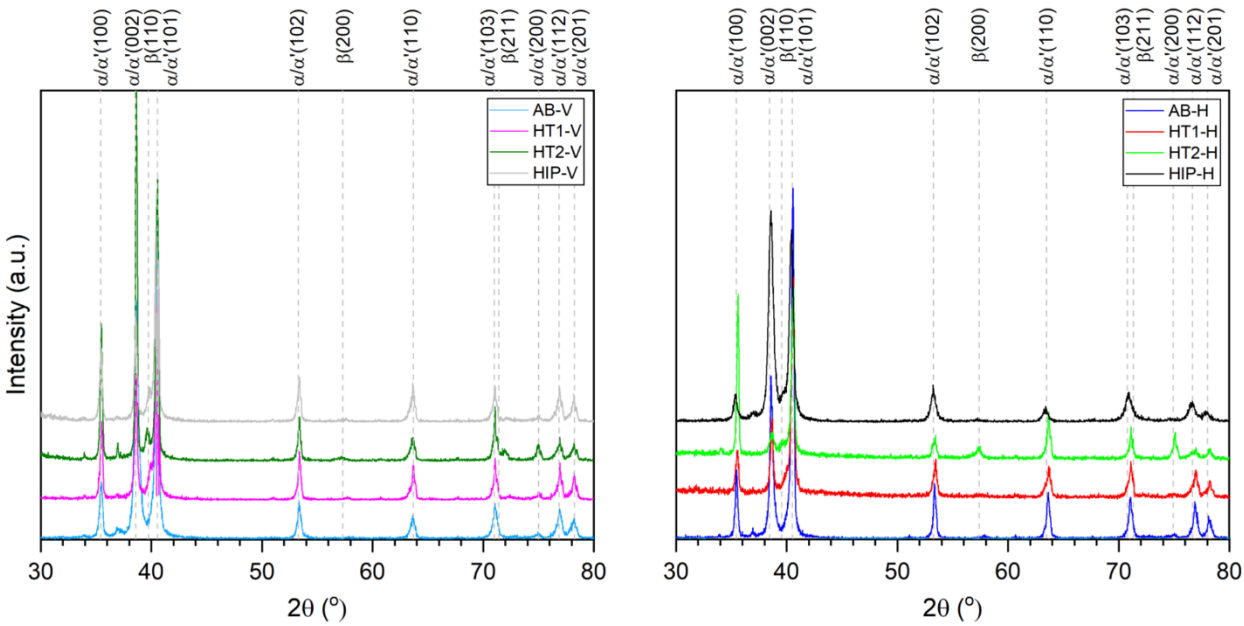


Figure 8. XRD patterns of the as-built and differently heat-treated L-PBF processed Ti-6Al-4V alloy; (left) vertical and (right) horizontal cross-sections.

3.3 Electrochemical analysis

3.3.1 Potentiodynamic polarization test

Electrochemical behavior of L-PBF processed Ti-6Al-4V parts were studied in a 3.5% NaCl solution to understand how microstructural evolution in differently heat-treated parts affect corrosion resistivity. The potentiodynamic polarization plots obtained from immersing the samples in the NaCl electrolyte are presented in Figure 9. By subjecting the samples to a potential scan of ±25 mV around their open circuit potential (OCP), a linear relationship between voltage and current was observed, with the slope of this relationship referred to as the polarization resistance (R_p) . The fitted results of potentiodynamic polarization curves are listed in Table 2.

The corrosion rate can be directly calculated by utilizing the equation below, which involves the surface-normalized corrosion current [26]:

$$v = K \times \frac{a.i_{corr}}{D}$$
 (Eq. 1)

 $v = K \times \frac{a.i_{corr}}{D}$ (Eq. 1) where K is a material constant (3272 $\frac{mm}{A.\ cm.\ year}$), a is the equivalent weight of the Ti-6Al-4V alloy (11.768 $\frac{g}{equiv}$), i_{corr} is the corrosion current ($\frac{\mu A}{cm^2}$), and D is the bulk density of Ti-6Al-4V alloy (4.45 $\frac{g}{cm^3}$). The calculated parameters are summarized in Table 2.

The electrochemical behavior of all samples, regardless of their cross-section orientation, exhibited corrosion potentials E_{corr} within the range of -0.12 to -0.058 V. A vertical anodic branch was observed in all specimens, indicating passivation behavior. The passivation current i_n represents the point at which the passivated region begins, and higher values of passivation current indicate a longer duration for the formation of the oxide film on the specimen's surface, which is undesirable. The passivation current for most samples ranged from approximately 4 to 5 $\frac{\mu A}{cm^2}$, except for the HT2-V sample (refer to Table 2). The higher corrosion rate observed in the vertical section of the HT2 sample may be attributed to the larger size of β grains in this sample. The EBSD data showed that mean size of the β grain in the xz section of HT2 specimen was approximately 2.5 times larger than that in the xy section. The presence of larger β grain sizes reduced formation of a uniform passive oxide film on the surface [45].

In the potential range of 1.75-2 V, all specimens exhibited an increase in current density (refer to Table 2). This range is considered as the break potential of the passive film (E_b). Several factors could explain this phenomenon, such as oxygen evolution on the surface, degradation and reformation of the oxide film, or the formation of another type of oxide within the TiO₂ matrix [62]. In the present study, the increase in current density could be attributed to a change in the electronic structure of the formed oxide film, indicating the occurrence of another type of oxidation process within the primary oxide film [63,64]. The subsequent vertical anodic branch observed after the change in the oxide film represents the repassivation of the sample. The range of potential at which a passive film forms, denoted as ΔE and shown in Figure 9, was found to be slightly broader in the HT1 specimens compared to the as-built and other heat-treatment conditions. No pitting was observed within the measured dataset up to a potential of approximately 2.5 V, indicating the stable formation of a passive film without any fluctuations in current density. This finding aligns with previous literature, which indicates that the pitting potential in the Ti-6Al-4V alloy can be as high as 2.5 V [65].

Regarding the corrosion rates, all the specimens are classified to be "very stable" based on the standard resistance class [26]. Although the microstructure of the as-built specimen showed differences in vertical (columnar grains) and horizontal (equiaxed grains) sections, the corrosion rate values were similar. This can be explained by non-equilibrium transformation of $\beta \rightarrow \alpha'$ due to the high cooling rate and formation of α' martensite as the dominant phase in the microstructure of the as-built samples. The applied heat-treatment and resultant evolution in microstructure altered the corrosion rate. At temperature of 850 °C (HT1), $\alpha + \beta$ was present in the microstructure with minimum growth of prior β grains. It was seen that the corrosion rate decreased from 2.08 × $10^{-3} \frac{mm}{year}$ (horizontal cross-section) and $2.06 \times 10^{-3} \frac{mm}{year}$ (vertical cross-section) in AB samples to $1.32 \times 10^{-3} \frac{mm}{year}$ (Horizontal cross-section) and $1.71 \frac{mm}{year}$ (vertical cross-section) in HT1 samples. Typically, the metastable α' phase in the L-PBF processed Ti-6Al-4V alloy becomes less stable when exposed to a corrosive environment.

Increasing temperature of post heat treatment can enhance β grains size after decomposition of α' phase. This coarsening of β grains leads to higher rate of alloying element segregation (vanadium in β , and aluminum in α) and less uniformity in the formed film, thus, compromises the integrity of the oxide film on the surface [66,67]. For the heat-treated conditions, the corrosion rate was lower in the xy section compared to the xz section, which could be associated with the equiaxed prior β grains (see Figure 4). Finally, the horizontal (xy) cross-section of the HT1 part had the lowest corrosion rate because of the more complete decomposition of the α' and presence of the nobler α and still extremely small β particles. In titanium alloys, β phase shows the highest corrosion resistance followed by the α and α' phases [23,32]. The small β particles do not compromise the integrity of the oxide film. Therefore, the small β particles along with the nobler α phase and equiaxed prior β grain structure resulted in a better corrosion resistance of the HT1-H sample amongst all other samples. However, despite the increased presence of β phase in the HT2 sample, there was no improvement in corrosion resistance, which can be attributed to the coarse grain size.

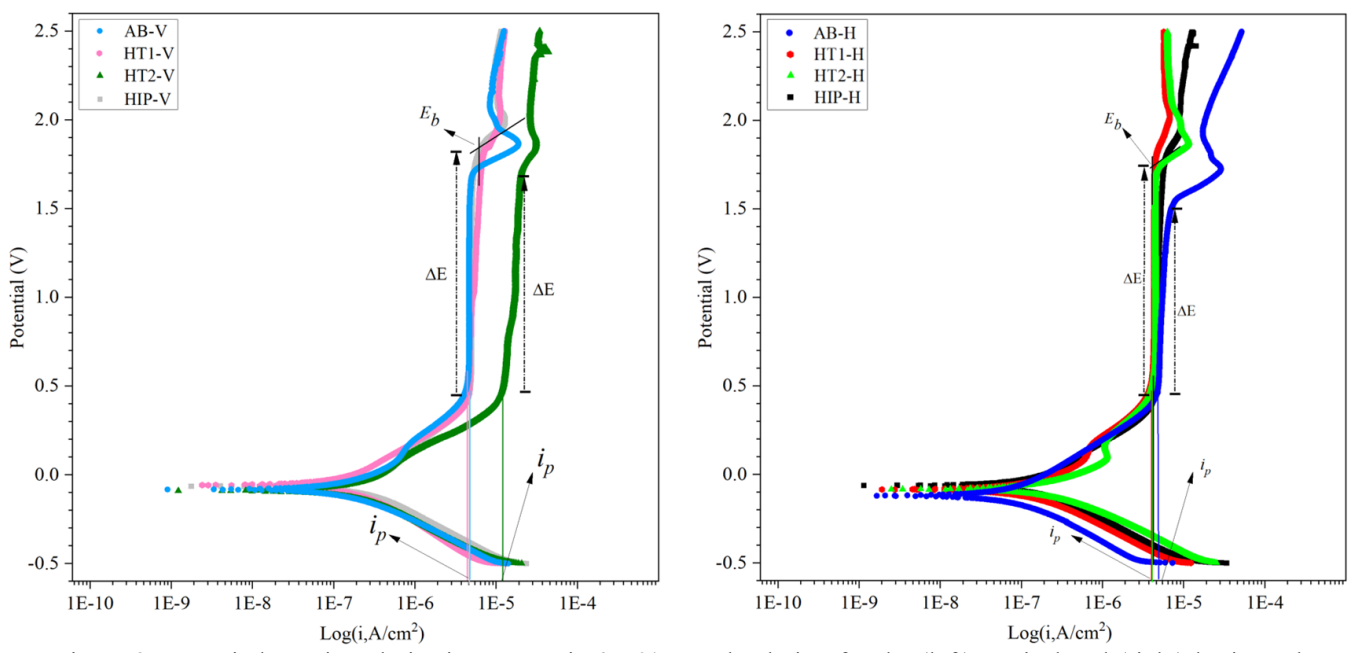


Figure 9. Potentiodynamic polarization curves in 3.5 % NaCl solution for the (left) vertical and (right) horizontal cross-sections of L-PBF processed HDH Ti-6Al-4V samples in as-built (AB) and differently heat-treated including annealing treatment at 850 °C (HT1), annealing treatment at 1045 °C (HT2), hot isostatically pressed at 899 °C (HIP) conditions.

Table 2. Analyzed data from the polarization test in 3.5 % NaCl solution collected from the as-build and differently

heat-treated L-PBF processed Ti-6Al-4V samples.

Sample	$i_{corr}(\frac{\mu A}{cm^2})$	E _{corr} (V)	$R_p(\frac{\Omega}{cm^2})$	E _b (V)	$i_p (\frac{\mu A}{cm^2})$	ΔΕ (V)	v (mm/year)
АВ-Н	0.240	-0.120	0.568	1.50	4.9	0.968	2.08×10^{-3}
НТ1-Н	0.153	-0.085	0.352	1.79	4.02	1.285	1.32×10^{-3}
НТ2-Н	0.190	-0.086	0.304	1.71	4.07	1.152	1.64×10^{-3}
HIP-H	0.215	-0.069	0.296	1.72	4.5	1.130	1.86×10^{-3}
AB-V	0.238	-0.083	0.293	1.67	4.3	1.115	2.06×10^{-3}
HT1-V	0.198	-0.058	0.328	1.75	4.7	1.280	1.71×10^{-3}
HT2-V	0.305	-0.119	0.282	1.60	12.4	1.092	2.64×10^{-3}
HIP-V	0.262	-0.085	0.241	1.74	4.8	1.183	2.27×10^{-3}

3.3.2 Electrochemical impedance spectroscopy

The EIS test was performed to evaluate the electrochemical behavior and stability of the formed oxide film after immersion in saline water, Figure 10. In the Nyquist plot shown in Figure 10a-b, the arc radius can be used to evaluate the polarization resistance of the parts. The HT1 sample exhibited a larger arc radius, suggesting a better polarization resistance [68]. Also, these findings support the PD data in which the higher heat-treatment temperatures diminished corrosion resistance (i.e., leading to smaller arc size) and the arc radius and corrosion resistivity followed the HT1>HIP>HT2 trend. Regarding the Bode plots in Figure 10c-d, at high frequencies of 10^3 - 10^5 Hz, the absolute impedance value (|Z|) reaches a plateau, and the phase angle drops to zero. By investigating intermediate frequencies ranging 10^0 - 10^3 Hz, it is evident that the phase angle approaches 90° which is an indicator of passivation behavior of the exposed L-PBF processed Ti-

6Al-4V surfaces to saline water which confirms the vertical anodic branch in the PD data (see Figure 9).

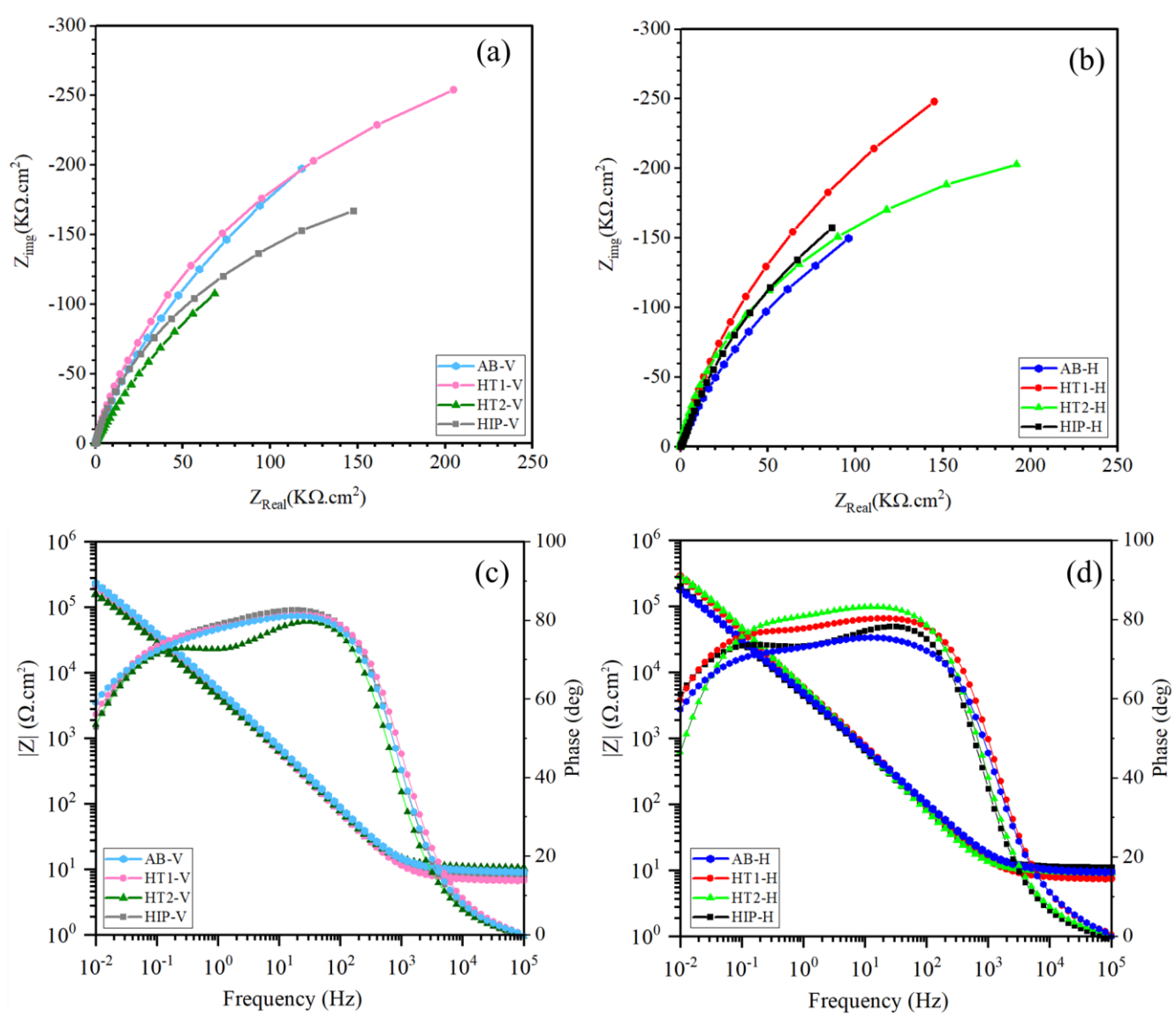


Figure 10. The EIS measurements for vertical and horizontal planes of the L-PBF processed HDH Ti-6Al-4V powder in AB, HT1, HT2, and HIP conditions tested in 3.5% NaCl solution: (a,b) Nyquist plots and (c,d) Bode plots.

Figure 11a-b shows the proposed electrical equivalent circuits used to fit to the EIS spectra, in which R_s is the solution resistance, R_{ct} is the barrier inner layer resistance, R_f is the porous layer resistivity, CPE_I is the porous outer layer capacitance, and CPE_{dl} is the barrier inner layer capacitance. The m and n values show the essence of the produced passivation films i.e., CPE is an ideal capacitor if m or n equal to 1, and CPE is an ideal resistor if m or n equal to 0. The obtained values for n were between 0 < n < 1 and they were close to 1, suggesting capacitive behavior for all samples. The summarized values of the fitting parameters obtained from analyzing the EIS data using the equivalent circuits mentioned above can be found in Table 3.

Table 3. The EIS fitting parameters for the xz and xy planes of L-PBF processed Ti-6Al-4V in AB, H	Γ1, HT2, and
HIP conditions.	

Sample	R_s $(K\Omega.cm^2)$	R_{ct} $(K\Omega.cm^2)$	CPE _{dl} (μF. cm ⁻²)	n	R_f (K Ω .cm ²)	CPE ₁ (μF. cm ⁻²)	m
АВ-Н	0.009544	645.90	10.47	0.66	18.1	38.11	0.86
НТ1-Н	0.00762	989.80	25.38	0.81	0.004	9.224	1
НТ2-Н	0.00950	497.50	11.23	0.79	0.002	21.03	0.96
HIP-H	0.007823	643.60	20.89	0.81	0.059	34.4	0.88
AB-V	0.009171	390.70	37.51	0.89	-	-	-
HT1-V	0.006766	412.40	41.99	0.89	-	-	-
HT2-V	0.01057	343.20	24.64	0.79	6.46	30.82	0.93
HIP-V	0.05656	361.60	38.05	0.90	-	-	-

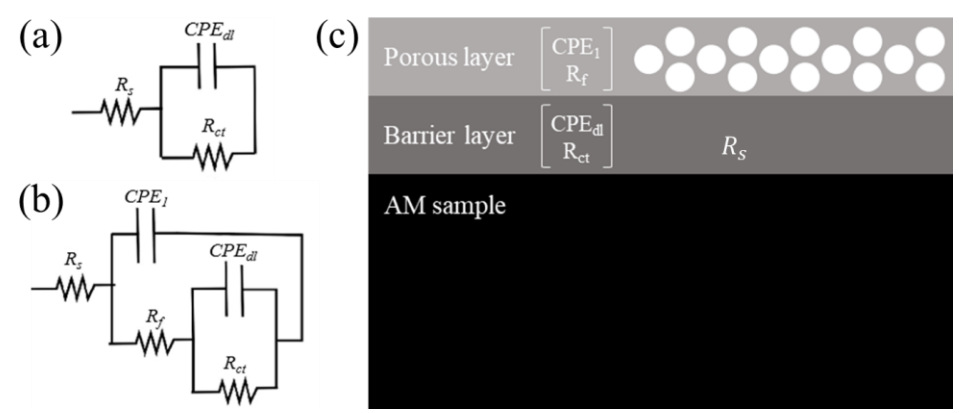


Figure 11. Equivalent circuit used for impedance spectra analysis with (a) one-time constant and (b) two-time constants. (c) Schematic of protective passive film with duplex structure formed on the L-PBF processed Ti-6Al-4V substrate.

Typically, EIS measurements are conducted on metal surfaces to analyze the surface state immersed in an electrolyte. In titanium alloys, the oxide layer is usually composed of two layers with a thin barrier inner layer and a porous outer layer which increase the layer/solution surface area (see Figure 11c) [69,70]. Thus, instead a mix of the conventional Randles equivalent circuit with one-time constant phase element (CPE_{dl}) – in which a thick barrier layer is assumed to form on surface – and in a few cases, an equivalent circuit with two constant phase elements (CPE_{l} and CPE_{dl}) were fitted to the EIS data to extract EIS parameters indicating formation of a barrier layer and porous film on top of it (see Figure 11a,b). In the vertical sections, the impedance spectra of AB, HT1 and HIP specimens were fitted by one-time constant phase element, while the impedance spectrum of HT2 was fitted by two-time constant phase elements. In the horizontal sections, the impedance spectra of all specimens were fitted by two-time constants. These findings aligned with the proposed equivalent circuits by Pan *et al.* [71] on the passive film formation of the exposed titanium alloys to saline water. In fact, when the outer passive film is thin and pores are filled with the electrolyte (see porous layer in Figure 11c), it can be assumed that the effect of the porous

layer on the electrochemical behavior is limited. Instead, the inner layer (or barrier layer in Figure 11c) dominates the impedance behavior during corrosion test and Randles equivalent circuit with one-time constant phase element is suitable.

As shown in Table 3, the resistivity of the inner barrier layer (R_{ct}) is notably higher than the porous layer (R_f), suggesting that the electrochemical behavior is mainly controlled by the inner barrier layer. Furthermore, lower frequencies (10^{-2} Hz) in Bode plot correlate with charge transfer (R_{ct}) of the oxide layer. Thus, the higher R_{ct} value corresponds with slower corrosion reaction on the sample surface because of higher interfacial charge-transfer resistance [72,73]. A thicker passive layer forms on regions in which the α phase is present and exposed to the electrolyte due to higher accelerated passivation tendency of this phase compared to α' and β phases [34]. The HT1 sample in both horizontal and vertical cross-sections demonstrated the best corrosion resistance as supported by the highest R_{ct} .

3.4 Analysis of the formed oxide film

Figure 12 depicts the XPS spectra of the Ti 2p region at different sputtering times, ranging from 0 s to 300 s, including intermediate times such as 10 s, 20 s, 40 s, 60 s, 120 s, and 300 s. The spectra exhibit the presence of three distinct valence states of titanium ions within the passive film: Ti⁴⁺, Ti³⁺, and Ti²⁺, indicating the coexistence of TiO₂, Ti₂O₃, and TiO. These results suggest that a non-equilibrium electrochemical reaction occurs at the surface, as the presence of multiple oxidation states is not typically expected in an ideal corrosion process. Notably, Ti⁴⁺ predominates in the electrochemical testing in 3.5 wt% NaCl. However, as the sputtering time increases, the proportions of Ti³⁺ and Ti²⁺ progressively rise while the fraction of Ti⁴⁺ diminishes. This observation suggests a conversion of Ti⁴⁺ to Ti³⁺ and Ti²⁺, with a higher concentration of Ti³⁺ and Ti²⁺ nearer to the film surface, indicating the non-equilibrium presence of oxygen. This phenomenon may indicate the diffusion-controlled behavior of oxygen at the interface between the surface and solution.

Table 4 presents the atomic percentages of titanium (Ti) ions in different valence states at various sputtering times. Initially, Ti⁴⁺ ions constitute 90.47 % of the passive film surface. However, as the sputtering time increases up to 300 s, the proportion of Ti⁴⁺ ions decreases to 35.28 %. Chloride ions (Cl⁻) in the saline water hinder the generation of Ti⁴⁺ ions. Additionally, vacancies can be developed when the adsorbed Cl ions enter oxygen vacancies through an autocatalytic effect [74]. These newly formed oxygen vacancies impede the conversion of Ti⁴⁺ ions to Ti³⁺ and Ti²⁺ ions, as demonstrated by the peak around 532 eV binding energy in the O 1s spectrum, which corresponds to off-lattice oxygen [75]. This peak is commonly referred to as the oxygen vacancy peak, despite the understanding that a missing oxygen atom cannot emit a photoelectron. The XPS spectra of the O 1s region also confirms a higher concentration of oxygen vacancies on the surface at shorter sputtering times [76,77]. After 10 s of sputtering, the fraction of Ti³⁺ ions increases in the passive film immersed in the saline water. Furthermore, after 60 s of sputtering, there is a slight increase in the fraction of Ti²⁺ ions, accompanied by a significant reduction in the fraction of Ti⁴⁺ ions. The literature suggests that suboxides including Ti₂O₃ and TiO can form at the passive film and the metal interface during the initial stages of corrosion, gradually transforming into the more stable TiO₂ [24,78,79]. Consequently, a lower concentration of TiO (6.03 %) is detected after 60 s of sputtering, in agreement with the results displayed in Figure 12. Additionally, the presence of Ti⁰ concentration after 300 s of sputtering suggests that the interaction of aluminum (Al) and/or vanadium (V) with oxygen vacancies is more favorable than that of titanium, resulting in the formation of metallic Ti.

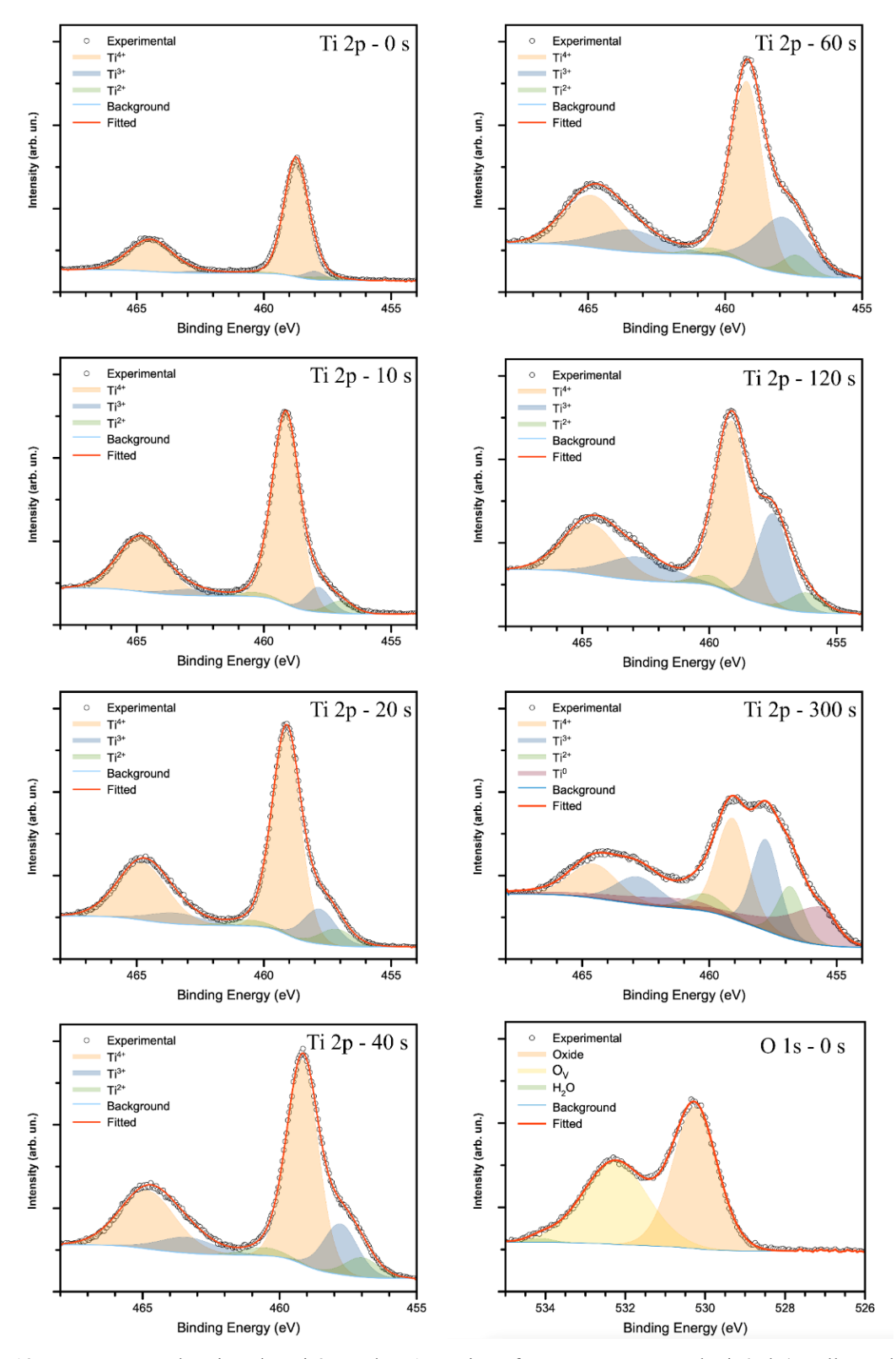


Figure 12. XPS spectra showing the Ti 2p and O 1s regions for L-PBF processed Ti-6Al-4V alloy. The data was collected after polarization tests in saline water. The alloy surface was sputtered using an Ar⁺ ion beam with different sputtering times to quantify the oxide film composition.

The XPS spectra of the O 1s region were analyzed to examine the passive film surfaces, and the resulting atomic percentages of different oxygen states are summarized in Table 4. As the sputtering time increases, the atomic percentage of oxygen vacancies (O_V) decreases, indicating a lack of interaction between chloride (Cl^-) ions and O_V on the lower surface, preventing the generation of new oxygen vacancies. The O 1s spectra were deconvolved into the metal-O-metal bond (O_L) or O 1s, the O_V bond, and absorbed water (H_2O). The peak corresponding to the O_L primarily originates from titanium oxide (TiO_2) which is related to the presence of highly concentrated Ti^{4+} in the passive film (Figure 12). The absorbed H_2O is highest after 300 s of sputtering, which may be related to the increased roughness on the sample surface due to pitting corrosion. Concurrently, the concentration of O_V decreased with prolonging sputtering. Further information on the XPS data can be found in the supplemental Tables 1 and 2.

The presented XPS analysis of the Ti 2p region confirms the gradual transition of TiO₂, Ti₂O₃, and TiO as the primary constituents of the passive film, progressing from the outer layer to the inner side of the formed oxide film. The formation of a passive oxide layer includes (1) formation of a thin layer TiO on Ti alloy, (2) oxidation of TiO to Ti₂O₃ which initiates the dehydration process, (3) transformation of Ti₂O₃ (trivalent state) into TiO(OH)₂ (tetravalent state), (4) dehydration of TiO(OH)₂ and formation of the most stable titanium oxide (TiO₂) at the outermost surface of the oxide film [9,80,81]. In this process, both TiO and Ti₂O₃ films which are present in the inner layers at the metal/film interface, will continuously form because of oxygen diffusion. Finally, the formation of the oxide film is accelerated by the presence of Cl⁻ ions, thus, rapidly covering the bare base plate with a passive film [82,83].

Table 4	The ator	nic ratio	of Ti and	10	valances a	t different	sputtering tin	166
1 aute 4.	THE ator	me rano	or ir and	ı	varances a	t different	spunering un	ies.

Sputter Time (s)	Ti ⁴⁺ (%at)	Ti ³⁺ (%at)	Ti ²⁺ (%at)	Ti ⁰ (%at)	O 1s (%at)	O _V (%at)	H ₂ O (%at)
0	90.47	5.41	4.13	0	53.38	45.82	0.80
10	85.15	9.59	5.26	0	59.69	36.06	4.25
20	76.68	16.08	7.24	0	65.96	34.04	0
40	72.93	19.60	7.47	0	71.10	28.90	0
60	62.85	31.12	6.03	0	70.50	29.50	0
120	60.41	32.65	6.93	0	71.68	28.32	0
300	35.28	25.40	14.18	25.14	72.60	27.40	0

3.5. Process-microstructure-electrochemistry relationships

Anisotropy in the anodic dissolution behavior of fusion-based AM processed Ti-6Al-4V alloys in a NaCl electrolyte can be attributed to the microstructure. This is primarily linked to the dominant presence of acicular α' phase in the fusion-based Ti-6Al-4V alloy, which negatively impacts corrosion resistance. The width of α/α' laths, the phase fraction of α/α' and β , and their distribution significantly influence the electrochemical behavior and corrosion rate. Decreasing the width of α -laths enhances corrosion resistance in a NaCl electrolyte. Surprisingly, the annealing treatment of Ti-6Al-4V did not result in inferior anodic dissolution resistance compared to the as-fabricated alloy, as reported by Li *et al.* [46], likely due to microstructural alterations affecting the anodic dissolution characteristics.

Scan strategy during L-PBF often lead to variations in microstructure and resultant properties in fusion-based AM metals [7,18,84,85]. Distinct microstructural characteristics and corrosion behavior were observed on different section planes of AM processed Ti-6Al-4V [28,32–34,36,46]. These microstructural dissimilarities are likely to cause variations in electrochemical corrosion resistance between different section planes, such as the horizontal (xy plane) and build direction (z plane). In this research, implementing a scan rotation of 67° transformed the initially columnar grain structure into grains with a more randomized orientation. This modification effectively reduced the inherent anisotropy of the L-PBF manufactured Ti-6Al-4V components and led to isotropic electrical behavior in different planes.

Fusion-based AM processed Ti-6Al-4V alloys often exhibit microstructural anisotropy and residual stress up to 150 MPa, which reduces corrosion resistance [33,46]. To mitigate the corrosion rate, relieving residual stress through stress relief treatment at 650 °C for 2 h is essential [86]. After this treatment, anodic dissolution behavior in AM processed Ti-6Al-4V alloy is attributed to microstructural characteristics [87] and solute partitioning among constituent phases [88]. Both increased grain size and homogenization of α -laths weaken resistance to dissolution. However, larger fractions of β can significantly enhance anodic dissolution resistance for Ti-6Al-4V, which is attributed to the superior stability of the passive film formed on β phase compared to α/α' phase. The composition-driven potential difference between α and β phases leads to the formation of galvanic cells. The extent of galvanic effect depends on solute concentration differences between the α/α' and β phases, which tends to decrease after heat treating below the β_{transus} temperature. This change was observed in conditions such as AB (after stress relief), HT1, and HIP treatments. The α/α' lath width measurements indicated that heat treatment above the β_{transus} temperature (HT2) led to a more uniform microstructure, coarser α lath width, and a higher fraction of β phase, resulting in a dominant galvanic effect, lower corrosion resistivity, and reduced corrosion resistance compared to other samples.

In general, the formation of a stable passive film on the surface of Ti-based alloys inhibits anodic dissolution. The presence of a thermodynamically stable TiO2 oxide layer plays a crucial role in improving the resistance to dissolution for Ti-based alloys. The thickness of the passive film is influenced by migration and diffusion rates in the oxide films and dissolution rates at the oxide films/electrolyte interface. The observed high passive film resistance, relatively low passive film capacitance derived from electrochemical impedance spectroscopy (EIS) at the corrosion potential (E_{corr}), and low corrosion rates indicate the stability of the passive film. X-ray photoelectron spectroscopy (XPS) results indicate that the passive film on L-PBF processed Ti-6Al-4V is mainly composed of a TiO₂ layer that is likely amorphous but includes hydrated TiO₂ at the oxide/solution interface and suboxides TiO and Ti₂O₃ in the lower layers at the metal/oxide interface.

When exposed to corrosive environment, Ti-based alloys possess a strong self-passivation ability because of formation of a passive film with a layer thickness up to 50 μ m and is capable of regenerating if disrupted [89]. Passive films naturally form on the surface of Ti-based alloys and effectively hinder the process of anodic dissolution. The presence of a thermodynamically stable TiO₂ oxide layer significantly contributes to enhancing the resistance against dissolution in Ti-based alloys [88]. The thickness of this passive film is typically influenced by factors such as the rate of migration and diffusion within the oxide films, as well as the dissolution rate at the interface of the oxide films and the electrolyte [90]. In this study, the strong resistance offered by the passive film, coupled with the relatively low passive film capacitance determined through EIS at the E_{corr} , along with the observed low corrosion rates, indicates the stability of this passive film. The XPS

results provided insight into the composition of the passive film on L-PBF processed Ti-6Al-4V, revealing a predominantly TiO₂ layer. This layer consists of hydrated TiO₂ at the interface between the oxide and the solution, and it also contains suboxides TiO and Ti₂O₃ in the underlying layers situated at the junction between the metal and the oxide. These observations agreed with earlier studies [23,24,31–33,36,45,46,88,91,92].

4. Conclusion

This study aimed at understanding the effect of post heat-treatment on texture and grain evolution as well as electrochemical behavior of the L-PBF fabricated hydride-dehydride non-spherical Ti-6Al-4V parts in saline water. The following conclusions are drawn:

- The applied scan rotation of 67 ° altered the fully columnar grains to more randomly oriented grains, thus, mitigating the anisotropic nature of the Ti-6Al-4V parts fabricated using L-PBF.
- Electrochemical studies showed a slight improvement in corrosion resistivity of the heattreated sample below β_{transus} temperature. The formation of nanoscale β phase alongside α phase expedited formation of a passive layer on the surface exposed to saline water. The calculated corrosion rates were in the range of $1.5\text{-}2 \times 10^{-3}$ mmpy, considered as a very stable oxide film formation on the exposed surface to 3.5 wt.% NaCl solution.
- By employing heat treatment to enhance the microstructure, uniform electrochemical characteristics were established between the horizontal and vertical orientations of L-PBF processed Ti-6Al-4V. Under a passivation potential of 0.45 V and a passive current density of $4.5 \,\mu\text{A.cm}^{-2}$, the material developed a passive film with a breakdown potential of $\sim 1.75 \,\text{V}$.
- The XPS analysis of passive film on L-PBF Ti-6Al-4V revealed a mixture of TiO₂, Ti₂O₃, and TiO, indicating a non-equilibrium electrochemical reaction. While Ti⁴⁺ dominates initially in 3.5 wt% NaCl, longer sputtering led to increased Ti³⁺ and Ti²⁺ proportions, implying a conversion of Ti⁴⁺ to lower oxidation states nearer to the surface due to non-equilibrium oxygen presence. This phenomenon might signify the diffusion-controlled movement of oxygen at the boundary between the surface and the surrounding solution.
- The constituent phases and their morphology evolved after heat-treatment at different conditions. The stress relief treatment at 650 °C on the as-built parts led to the appearance of trace amounts of nanoscale β phase in α' martensite. By increasing the temperature to sub-(850 °C HT1) and above (1045 °C HT2) β_{transus} temperature, α' → α+β phase transformation was documented with optical and scanning electron microscopy. HIP treatment at ~900 °C resulted in a similar microstructure as in HT1 with slightly larger β particles.

Acknowledgements

AM acknowledges the startup funding provided by the Mechanical, Materials, and Aerospace Engineering Department at the Illinois Institute of Technology in Chicago, Illinois. The authors acknowledge partial support from the National Science Foundation under grant number DMR-2050916. Additionally, this research received support from the Pennsylvania Infrastructure Technology Alliance, which is a collaboration between Carnegie Mellon University, Lehigh University, and the Department of Community and Economic Development (DCED) of the Commonwealth of Pennsylvania. The authors extend their gratitude to Reading Alloys (now part of Kymera International) and Mike Marucci for supplying the Ti-6Al-4V powder used in this study and for their valuable assistance. Special thanks are also given to Dr. Ziheng Wu for his assistance with the part production process at CMU.

References

- [1] C. Cui, B. Hu, L. Zhao, S. Liu, Titanium alloy production technology, market prospects and industry development, Mater. Des. 32 (2011) 1684–1691.
- [2] M.J. Donachie, Titanium: a technical guide, (2000).
- [3] Z. Liu, C. Huang, C. Gao, R. Liu, J. Chen, Z. Xiao, Characterization of Ti6Al4V powders produced by different methods for selective electron beam melting, J. Min. Metall. Sect. B Metall. 55 (2019) 121–128.
- [4] J.M. Benson, E. Snyders, the Need for Powder Characterisation in the Additive Manufacturing, South African J. Ind. Eng. 26 (2015) 104–114.
- [5] I.E. Anderson, E.M.H. White, R. Dehoff, Feedstock powder processing research needs for additive manufacturing development, Curr. Opin. Solid State Mater. Sci. 22 (2018) 1–8.
- [6] U. and U. Fritsching, V. Uhlenwinkel, Hybrid Gas Atomization for Powder Production, 2012.
- [7] A. Mostafaei, C. Zhao, Y. He, S. Reza Ghiaasiaan, B. Shi, S. Shao, N. Shamsaei, Z. Wu, N. Kouraytem, T. Sun, J. Pauza, J. V. Gordon, B. Webler, N.D. Parab, M. Asherloo, Q. Guo, L. Chen, A.D. Rollett, Defects and anomalies in powder bed fusion metal additive manufacturing, Curr. Opin. Solid State Mater. Sci. 26 (2022) 100974.
- [8] Y.Y. Sun, S. Gulizia, C.H. Oh, C. Doblin, Y.F. Yang, M. Qian, Manipulation and Characterization of a Novel Titanium Powder Precursor for Additive Manufacturing Applications, JOM. 67 (2015) 564–572.
- [9] W. Ding, G. Chen, M. Qin, Y. He, X. Qu, Low-cost Ti powders for additive manufacturing treated by fluidized bed, Powder Technol. 350 (2019) 117–122.
- [10] A. Loukanov, N. El Allaoui, A. Omor, F.Z. Elmadani, K. Bouayad, N. Seiichiro, Oxidation behavior of low-cost CP-Ti powders for additive manufacturing via fluidizatio, J. Neurol. Sci. (2020) 116544.
- [11] Y.P. Dong, Y.L. Li, S.Y. Zhou, Y.H. Zhou, M.S. Dargusch, H.X. Peng, M. Yan, Costaffordable Ti-6Al-4V for additive manufacturing: Powder modification, compositional modulation and laser in-situ alloying, Addit. Manuf. (2020) 101699.
- [12] Opportunities for Low Cost Titanium in Reduced Fuel Consumption, Improved Emissions, and Enhanced Durability Heavy-duty Vehicles, 2002.
- [13] H. Fayazfar, M. Salarian, A. Rogalsky, D. Sarker, P. Russo, V. Paserin, E. Toyserkani, A critical review of powder-based additive manufacturing of ferrous alloys: Process parameters, microstructure and mechanical properties, Mater. Des. 144 (2018) 98–128.
- [14] J. Varela, E. Arrieta, M. Paliwal, M. Marucci, J.H. Sandoval, J.A. Gonzalez, B. McWilliams, L.E. Murr, R.B. Wicker, F. Medina, Investigation of Microstructure and Mechanical Properties for Ti-6Al-4V Alloy Parts Produced Using Non-Spherical Precursor Powder by Laser Powder Bed Fusion, Materials (Basel). 14 (2021) 3028.
- [15] S.P. Narra, Z. Wu, R. Patel, J. Capone, M. Paliwal, J. Beuth, A.D. Rollett, Use of Non-Spherical Hydride-DeHydride (HDH) Powders in Powder Bed Fusion Additive Manufacturing, Addit. Manuf. 34 (2020) 101188.
- [16] Z. Wu, M. Asherloo, R. Jiang, M.H. Delpazir, N. Sivakumar, M. Paliwal, J. Capone, B. Gould, A. Rollett, A. Mostafaei, Study of Printability and Porosity Formation in Laser Powder Bed Fusion Built Hydride-Dehydride (HDH) Ti-6Al-4V, Addit. Manuf. 47 (2021) 102323.
- [17] M. Asherloo, Z. Wu, E. Ghebreiesus, S. Fryzlewicz, R. Jiang, B. Gould, M. Heim, D. Nelson, M. Marucci, M. Paliwal, A.D. Rollett, A. Mostafaei, Laser-beam powder bed

- fusion of cost-effective non-spherical hydride-dehydride Ti-6Al-4V alloy, Addit. Manuf. 56 (2022) 102875.
- [18] L. Thijs, F. Verhaeghe, T. Craeghs, J. Van Humbeeck, J.P. Kruth, A study of the microstructural evolution during selective laser melting of Ti-6Al-4V, Acta Mater. 58 (2010) 3303–3312.
- [19] J. Yang, H. Yu, J. Yin, M. Gao, Z. Wang, X. Zeng, Formation and control of martensite in Ti-6Al-4V alloy produced by selective laser melting, 108 (2016) 308–318.
- [20] S. Liu, Y.C. Shin, Additive manufacturing of Ti6Al4V alloy: A review, Mater. Des. 164 (2019) 107552.
- [21] H. Zhang, W. Qin, C. Man, H. Cui, D. Kong, Z. Cui, X. Wang, C. Dong, Effect of heat treatment on microstructure and corrosion behavior of Ti6Al4V fabricated by laser beam powder bed fusion, Corros. Sci. 209 (2022) 110789.
- [22] F.R. Kaschel, R.K. Vijayaraghavan, A. Shmeliov, E.K. McCarthy, M. Canavan, P.J. McNally, D.P. Dowling, V. Nicolosi, M. Celikin, Mechanism of stress relaxation and phase transformation in additively manufactured Ti-6Al-4V via in situ high temperature XRD and TEM analyses, Acta Mater. 188 (2020) 720–732.
- [23] A. Sharma, M.C. Oh, J.T. Kim, A.K. Srivastava, B. Ahn, Investigation of electrochemical corrosion behavior of additive manufactured Ti–6Al–4V alloy for medical implants in different electrolytes, J. Alloys Compd. 830 (2020) 154620.
- [24] P. Qin, L.Y. Chen, Y.J. Liu, Z. Jia, S.X. Liang, C.H. Zhao, H. Sun, L.C. Zhang, Corrosion and passivation behavior of laser powder bed fusion produced Ti-6Al-4V in static/dynamic NaCl solutions with different concentrations, Corros. Sci. 191 (2021) 109728.
- [25] A. Hemmasian Ettefagh, C. Zeng, S. Guo, J. Raush, Corrosion behavior of additively manufactured Ti-6Al-4V parts and the effect of post annealing, Addit. Manuf. 28 (2019) 252–258.
- [26] J. Yang, H. Yang, H. Yu, Z. Wang, X. Zeng, Corrosion Behavior of Additive Manufactured Ti-6Al-4V Alloy in NaCl Solution, Metall. Mater. Trans. A. 48 (2017) 1–11.
- [27] H.M. Hamza, K.M. Deen, W. Haider, Microstructural examination and corrosion behavior of selective laser melted and conventionally manufactured Ti6Al4V for dental applications, Mater. Sci. Eng. C. 113 (2020) 110980.
- [28] H. Zhang, C. Man, C. Dong, L. Wang, W. Li, D. Kong, L. Wang, X. Wang, The corrosion behavior of Ti6Al4V fabricated by selective laser melting in the artificial saliva with different fluoride concentrations and pH values, Corros. Sci. 179 (2021) 109097.
- [29] A. Leon, G.K. Levy, T. Ron, A. Shirizly, E. Aghion, The effect of hot isostatic pressure on the corrosion performance of Ti-6Al-4 V produced by an electron-beam melting additive manufacturing process, Addit. Manuf. 33 (2020) 101039.
- [30] L. Mo, P. Dennis, P. Tobias, M.-J. Hadi, Influence of Heat Treatment and Surface Finishing on the Corrosion Behavior of Additive Manufactured Ti-6Al-4V, Adv. Metall. Mater. Eng. 3 (2020) 81–94.
- [31] X. Yang, X. Dong, W. Li, W. Feng, Y. Xu, Effect of solution and aging treatments on corrosion performance of laser solid formed Ti-6Al-4V alloy in a 3.5 wt. % NaCl solution, J. Mater. Res. Technol. 9 (2020) 1559–1568.
- [32] N. Dai, L.-C.C. Zhang, J. Zhang, Q. Chen, M. Wu, Corrosion behavior of selective laser melted Ti-6Al-4 V alloy in NaCl solution, Corros. Sci. 102 (2016) 484–489.

- [33] N. Dai, L.-C.C. Zhang, J. Zhang, X. Zhang, Q. Ni, Y. Chen, M. Wu, C. Yang, Distinction in corrosion resistance of selective laser melted Ti-6Al-4V alloy on different planes, Corros. Sci. 111 (2016) 703–710.
- [34] B. Wu, Z. Pan, S. Li, D. Cuiuri, D. Ding, H. Li, The anisotropic corrosion behaviour of wire arc additive manufactured Ti-6Al-4V alloy in 3.5% NaCl solution, Corros. Sci. 137 (2018) 176–183.
- [35] J. Li, X. Lin, Y. Yang, J. Wang, J. Liu, P. Guo, W. Huang, Distinction in electrochemical behaviour of Ti6Al4V alloy produced by direct energy deposition and forging, J. Alloys Compd. 860 (2021) 157912.
- [36] J. Li, X. Lin, M. Zheng, J. Wang, P. Guo, T. Qin, M. Zhu, W. Huang, H. Yang, Distinction in anodic dissolution behavior on different planes of laser solid formed Ti-6Al-4V alloy, Electrochim. Acta. 283 (2018) 1482–1489.
- [37] M. Asherloo, Z. Wu, M. Heim, D. Nelson, M. Paliwal, A.D. Rollett, A. Mostafaei, Fatigue performance of laser powder bed fusion hydride-dehydride Ti-6Al-4V powder, Addit. Manuf. 59 (2022) 103117.
- [38] A. Shaikh, S. Kirwai, A. Patil, A. Shaikh, S. Kumar, ScienceDirect ScienceDirect ScienceDirect Effect of Temperature and Cooling Rates on the α + β Morphology of Effect of Temperature and Cooling Rates on the α + β Morphology of Ti-6Al-4V Alloy Ti-6Al-4V Alloy, Procedia Struct. Integr. 14 (2019) 782–789.
- [39] F. Bachmann, R. Hielscher, H. Schaeben, Texture Analysis with MTEX Free and Open Source Software Toolbox, Solid State Phenom. 160 (2010) 63–68.
- [40] M.C. Biesinger, L.W.M. Lau, A.R. Gerson, R.S.C. Smart, Resolving surface chemical states in XPS analysis of first row transition metals, oxides and hydroxides: Sc, Ti, V, Cu and Zn, Appl. Surf. Sci. 257 (2010) 887–898.
- [41] M.C. Biesinger, L.W.M. Lau, A.R. Gerson, R.S.C. Smart, Resolving surface chemical states in XPS analysis of first row transition metals, oxides and hydroxides: Sc, Ti, V, Cu and Zn, Appl. Surf. Sci. 257 (2010) 887–898.
- [42] S.A. Oh, R.E. Lim, J.W. Aroh, A.C. Chuang, B.J. Gould, B. Amin-Ahmadi, J. V. Bernier, T. Sun, P.C. Pistorius, R.M. Suter, A. D.Rollett, High speed synchrotron X-ray diffraction experiments resolve microsation in laser processed Ti-6Al-4Vtructure and phase transform, Mater. Res. Lett. 9 (2021) 429–436.
- [43] Z. Ye, W. Yang, L. Shu, Z. Wang, Q. Liu, Q. Yan, J. Wei, K. Zhang, F. Gou, The Investigation of Corrosion Behaviors of Type 316L Stainless Steel in Stagnating Liquid Lithium, Fusion Sci. Technol. 76 (2020) 157–162.
- [44] X. Zhang, H. Xu, Z. Li, A. Dong, D. Du, L. Lei, G. Zhang, D. Wang, G. Zhu, B. Sun, Effect of the scanning strategy on microstructure and mechanical anisotropy of Hastelloy X superalloy produced by Laser Powder Bed Fusion, Mater. Charact. 173 (2021) 110951.
- [45] G.A. Longhitano, M.A. Arenas, A. Conde, M.A. Larosa, A.L. Jardini, C.A. de C. Zavaglia, J.J. Damborenea, Heat treatments effects on functionalization and corrosion behavior of Ti-6Al-4V ELI alloy made by additive manufacturing, J. Alloys Compd. 765 (2018) 961–968.
- [46] J. Li, X. Lin, J. Wang, M. Zheng, P. Guo, Y. Zhang, Y. Ren, J. Liu, W. Huang, Effect of stress-relief annealing on anodic dissolution behaviour of additive manufactured Ti-6Al-4V via laser solid forming, Corros. Sci. 153 (2019) 314–326.
- [47] H. Yu, W. Li, S. Li, H. Zou, T. Zhai, L. Liu, Study on Transformation Mechanism and Kinetics of α' Martensite in TC4 Alloy Isothermal Aging Process, Cryst. . 10 (2020).

- [48] Seunghee A. Oh, J.W. Aroh, N. Lamprinakos, A.C. Chuang, A. Bucsek, R.M. Suter, A.D. Rollett, Study of martensite decomposition in Ti-6Al-4V under rapid heating via in situ synchrotron x-ray diffraction, submitted (2023).
- [49] N. Kazantseva, P. Krakhmalev, M. Thuvander, I. Yadroitsev, N. Vinogradova, I. Ezhov, Martensitic transformations in Ti-6Al-4V (ELI) alloy manufactured by 3D Printing, Mater. Charact. 146 (2018) 101–112.
- [50] J.G. Pauza, W.A. Tayon, A.D. Rollett, Computer simulation of microstructure development in powder-bed additive manufacturing with crystallographic texture, Model. Simul. Mater. Sci. Eng. 29 (2021) 55019.
- [51] R. Jiang, Z. Ren, J. Aroh, A. Mostafaei, B. Gould, T. Sun, A.D. Rollett, Quantifying Equiaxed vs Epitaxial Solidification in Laser Melting of CMSX-4 Single Crystal Superalloy, Metall. Mater. Trans. A Phys. Metall. Mater. Sci. 54 (2023) 808–822.
- [52] E. Fereiduni, A. Ghasemi, M. Elbestawi, Unique opportunities for microstructure engineering via trace B4C addition to Ti-6Al-4V through laser powder bed fusion process: As-built and heat-treated scenarios, Addit. Manuf. 50 (2022) 102557.
- [53] W.G. Burgers, On the process of transition of the cubic-body-centered modification into the hexagonal-close-packed modification of zirconium, Physica. 1 (1934) 561–586.
- [54] S.C. Wang, M. Aindow, M.J. Starink, Effect of self-accommodation on α/α boundary populations in pure titanium, Acta Mater. 51 (2003) 2485–2503.
- [55] R.H. Ericksen, R. Taggart, D.H. Polonis, The martensite transformation in Ti-Cr binary alloys, Acta Metall. 17 (1969) 553–564.
- [56] H. Beladi, Q. Chao, G.S. Rohrer, Variant selection and intervariant crystallographic planes distribution in martensite in a Ti–6Al–4V alloy, Acta Mater. 80 (2014) 478–489.
- [57] J. Zhang, X. Li, D. Xu, R. Yang, Recent progress in the simulation of microstructure evolution in titanium alloys, Prog. Nat. Sci. Mater. Int. 29 (2019) 295–304.
- [58] M. Asherloo, J. Hwang, R. Leroux, Z. Wu, K. Fezzaa, M. Paliwal, A.D. Rollett, A. Mostafaei, Understanding process-microstructure-property relationships in laser powder bed fusion of non-spherical Ti-6Al-4V powder, Mater. Charact. 198 (2023) 112757.
- [59] M. Asherloo, Z. Wu, J.E.C. Sabisch, I. Ghamarian, A.D. Rollett, A. Mostafaei, Variant selection in laser powder bed fusion of non-spherical Ti-6Al-4V powder, J. Mater. Sci. Technol. 147 (2023) 56–67.
- [60] P. Tarín, A. Gualo, A.G. Simón, N.M. Piris, J.M. Badía, Study of Alpha-Beta Transformation in Ti-6Al-4V-ELI. Mechanical and Microstructural Characteristics, Mater. Sci. Forum. 638–642 (2010) 712–717.
- [61] D. Xi, J. Wang, X. Guo, Influence of Heat Treatment Parameters on the Corrosion Resistance of Additively Manufactured Ti–6Al–4V Alloy, Biosci. Rep. (2009).
- [62] P. Acevedo-Peña, G. Vázquez, D. Laverde, J.E. Pedraza-Rosas, I. González, Influence of structural transformations over the electrochemical behavior of Ti anodic films grown in 0.1 M NaOH, J. Solid State Electrochem. 14 (2010) 757–767.
- [63] C. Vasilescu, S.I. Drob, J.M. Calderon Moreno, P. Osiceanu, M. Popa, E. Vasilescu, M. Marcu, P. Drob, Long-term corrosion resistance of new Ti–Ta–Zr alloy in simulated physiological fluids by electrochemical and surface analysis methods, Corros. Sci. 93 (2015) 310–323.
- [64] V.A. Alves, R.Q. Reis, I.C.B. Santos, D.G. Souza, T. de F. Gonçalves, M.A. Pereira-da-Silva, A. Rossi, L.A. da Silva, In situ impedance spectroscopy study of the electrochemical corrosion of Ti and Ti–6Al–4V in simulated body fluid at 25°C and 37°C,

- Corros. Sci. 51 (2009) 2473–2482.
- [65] J.J. de Damborenea, M.A. Larosa, M.A. Arenas, J.M. Hern??ndez-L??pez, A.L. Jardini, M.C.F. Ierardi, C.A.C. Zavaglia, R.M. Filho, A. Conde, Functionalization of Ti6Al4V scaffolds produced by direct metal laser for biomedical applications, Mater. Des. 83 (2015) 6–13.
- [66] M. Atapour, A. Pilchak, G.S. Frankel, J.C. Williams, M.H. Fathi, M. Shamanian, Corrosion Behavior of Ti-6Al-4V with Different Thermomechanical Treatments and Microstructures, Corrosion. 66 (2010) 065004-065004-9.
- [67] I. Cvijović-Alagić, Z. Cvijović, J. Bajat, M. Rakin, Composition and processing effects on the electrochemical characteristics of biomedical titanium alloys, Corros. Sci. 83 (2014) 245–254.
- [68] M.P. Pujadó, Carbon nanotubes as platforms for biosensors with electrochemical and electronic transduction, Springer Science & Business Media, 2012.
- [69] R. Chelariu, G. Bolat, J. Izquierdo, D. Mareci, D.M. Gordin, T. Gloriant, R.M. Souto, Metastable beta Ti-Nb-Mo alloys with improved corrosion resistance in saline solution, Electrochim. Acta. 137 (2014) 280–289.
- [70] G. Bolat, D. Mareci, R. Chelariu, J. Izquierdo, S. González, R.M. Souto, Investigation of the electrochemical behaviour of TiMo alloys in simulated physiological solutions, Electrochim. Acta. 113 (2013) 470–480.
- [71] J. Pan, D. Thierry, C. Leygraf, Electrochemical impedance spectroscopy study of the passive oxide film on titanium for implant application, Electrochim. Acta. 41 (1996) 1143–1153.
- [72] H. Wang, C. Yu, S. Wang, J. Gao, Electrochemical Corrosion Behavior and Prediction of Corrosion Rate for Low Alloy Steel after Tempering Treatment, Int. J. Electrochem. Sci. 10 (2015) 1169–1185.
- [73] A.B. Oliveira, A.C. Bastos, C.M. Fernandes, C.M.S. Pinho, A.M.R. Senos, E. Soares, J. Sacramento, M.L. Zheludkevich, M.G.S. Ferreira, Corrosion behaviour of WC-10% AISI 304 cemented carbides, Corros. Sci. 100 (2015) 322–331.
- [74] T. Qin, X. Lin, J. Yu, M. Wang, P. Guo, J. Li, Y. Zhang, J. Liu, S. Zhang, W. Huang, Performance of different microstructure on electrochemical behaviors of laser solid formed Ti–6Al–4V alloy in NaCl solution, Corros. Sci. 185 (2021) 109392.
- [75] T.J. Frankcombe, Y. Liu, Interpretation of Oxygen 1s X-ray Photoelectron Spectroscopy of ZnO, Chem. Mater. (2023).
- [76] H. Idriss, On the wrong assignment of the XPS O1s signal at 531–532 eV attributed to oxygen vacancies in photo- and electro-catalysts for water splitting and other materials applications, Surf. Sci. 712 (2021) 121894.
- [77] S. Nasiri Khalil Abad, J. Moghaddam, M. Mozammel, A. Mostafaei, M. Chmielus, Growth mechanism and charge transport properties of hybrid Au/ZnO nanoprisms, J. Alloys Compd. 777 (2019) 1386–1395.
- [78] A. Gebert, S. Oswald, A. Helth, A. Voss, P.F. Gostin, M. Rohnke, J. Janek, M. Calin, J. Eckert, Effect of indium (In) on corrosion and passivity of a beta-type Ti–Nb alloy in Ringer's solution, Appl. Surf. Sci. 335 (2015) 213–222.
- [79] W. Ding, Z. Wang, G. Chen, W. Cai, C. Zhang, Q. Tao, X. Qu, M. Qin, Oxidation behavior of low-cost CP-Ti powders for additive manufacturing via fluidization, Corros. Sci. 178 (2021) 109080.
- [80] M. Metikoš-Huković, A. Kwokal, J. Piljac, The influence of niobium and vanadium on

- passivity of titanium-based implants in physiological solution, Biomaterials. 24 (2003) 3765–3775.
- [81] T. Hanawa, K. Asami, K. Asaoka, Repassivation of titanium and surface oxide film regenerated in simulated bioliquid., J. Biomed. Mater. Res. 40 (1998) 530–538.
- [82] Y. Lu, J. Dong, W. Ke, Effects of Cl– Ions on the Corrosion Behaviour of Low Alloy Steel in Deaerated Bicarbonate Solutions, J. Mater. Sci. Technol. 32 (2016) 341–348.
- [83] Y. Ma, Y. Li, F. Wang, Corrosion of low carbon steel in atmospheric environments of different chloride content, Corros. Sci. 51 (2009) 997–1006.
- [84] R. Wauthle, B. Vrancken, B. Beynaerts, K. Jorissen, J. Schrooten, J.P. Kruth, J. Van Humbeeck, Effects of build orientation and heat treatment on the microstructure and mechanical properties of selective laser melted Ti6Al4V lattice structures, Addit. Manuf. 5 (2015) 77–84.
- [85] A. Mostafaei, R. Ghiaasiaan, I.-T. Ho, S. Strayer, K.-C. Chang, N. Shamsaei, S. Shao, S. Paul, A.-C. Yeh, S. Tin, A.C. To, Additive Manufacturing of Nickel-based superalloys: a state-of-the-art review on process-structure-defect-property relationship, Prog. Mater. Sci. 136 (2023) 101108.
- [86] S.A. Etesami, B. Fotovvati, E. Asadi, Heat treatment of Ti-6Al-4V alloy manufactured by laser-based powder-bed fusion: Process, microstructures, and mechanical properties correlations, J. Alloys Compd. 895 (2022) 162618.
- [87] S. Gollapudi, Grain size distribution effects on the corrosion behaviour of materials, Corros. Sci. 62 (2012) 90–94.
- [88] M. Geetha, U. Kamachi Mudali, A.K. Gogia, R. Asokamani, B. Raj, Influence of microstructure and alloying elements on corrosion behavior of Ti-13Nb-13Zr alloy, Corros. Sci. 46 (2004) 877–892.
- [89] J. Brezinová, R. Hudák, A. Guzanová, D. Draganovská, G. Ižaríková, J. Koncz, Direct metal laser sintering of Ti6Al4V for biomedical applications: Microstructure, corrosion properties, and mechanical treatment of implants, Metals (Basel). 6 (2016).
- [90] T. Ohtsuka, Growth of passive oxide films on iron and titanium under non-stationary state, Corros. Rev. 36 (2018) 87–104.
- [91] J.R. Chen, W.T. Tsai, In situ corrosion monitoring of Ti-6Al-4V alloy in H2SO 4/HCl mixed solution using electrochemical AFM, Electrochim. Acta. 56 (2011) 1746–1751.
- [92] G. Zhang, N. Li, J. Gao, H. Xiong, H. Yu, H. Yuan, Wire-fed electron beam directed energy deposition of Ti–6Al–2Zr–1Mo–1V alloy and the effect of annealing on the microstructure, texture, and anisotropy of tensile properties, Addit. Manuf. 49 (2022) 102511.

Supplementary Table 1: Summary of the peak position, full width at half maximum (FWHM), and surface area related to the fitted lines on Ti 2p spectrum. Data is for the 1 kV beam voltage.

elated to the	ne fitted lines o	on Ti 2p spectr	um. Data is fo	or the 1 kV be	eam voltage.			
0 s								
	Ti ⁴⁺ 3/2	Ti ⁴⁺ 1/2	Ti ³⁺ 3/2	Ti ³⁺ 1/2	Ti ²⁺ 3/2	Ti ²⁺ 1/2	Ti ⁰ 3/2	Ti ⁰ 1/2
Position	458.75	464.46	458.00	462.53	457.50	460.23	N/A	N/A
FWHM	1.10	2.02	0.90	2.20	1.50	1.80	N/A	N/A
Area	8387.60	4193.80	501.11	250.55	382.44	191.22	N/A	N/A
10 s								
Position	459.14	464.81	457.86	462.87	457.00	460.35	N/A	N/A
FWHM	1.27	2.20	1.10	2.20	1.20	1.80	N/A	N/A
Area	15829.51	7914.76	1782.44	891.22	977.74	488.87	N/A	N/A
20 s		•	•	•	•		•	•
Position	457.82	463.48	459.12	464.78	457.17	460.57	N/A	N/A
FWHM	1.5	2.4	1.31	2.32	1.5	2.12	N/A	N/A
Area	3609.46	1804.73	17215.17	8607.58	1625.57	812.79	N/A	N/A
40 s					•		•	•
Position	459.16	464.82	457.78	463.38	457	460.58	N/A	N/A
FWHM	1.36	2.38	1.46	2.36	1.45	1.76	N/A	N/A
Area	17994.46	8997.23	4835.69	2417.84	1841.8	920.9	N/A	N/A
60 s					•		•	•
Position	459.21	464.87	457.87	463.47	457.4	460.57	N/A	N/A
FWHM	1.37	2.38	2.21	2.83	1.2	1.75	N/A	N/A
Area	16142.03	8071.02	7993.52	3996.76	1549.48	774.74	N/A	N/A
120 s		•	•	•	•		•	•
Position	459.12	464.68	457.51	462.79	456.2	459.95	N/A	N/A
FWHM	1.5	2.53	1.5	3	1.5	1.5	N/A	N/A
Area	16777.63	8388.82	9067.71	4533.86	1925.6	962.8	N/A	N/A
300 s	•	•	•	•	•	•	•	•
Position	459.09	464.55	457.79	462.82	456.82	460.14	455.61	461.01
FWHM	1.48	2.17	1.25	2.08	1.21	1.83	1.45	2.82
Area	10284.91	5142.46	7405.29	3702.65	4132.11	2066.06	7326.75	3663.37

Supplementary Table 2: Summary of the peak position, full width at half maximum (FWHM), and surface area related to the fitted lines on O 1s spectrum. Data is for the 1 kV beam voltage.

0 s								
	O 1s	O_V	H ₂ O					
Position	530.25	532.26	534.10					
FWHM	1.31	1.91	0.70					
Area	11911.98	10224	179.58					